



**I
N
A
O
E**

**Development of computational algorithms
for the analysis of contrast images in laser
speckle imaging**

by

M.Sc. Eduardo Morales Vargas

Ph.D Research thesis

Instituto Nacional de Astrofísica, Óptica y Electrónica

January, 2022

Tonantzintla, Puebla

Advisors:

PhD. Hayde Peregrina Barreto

PhD. Julio Cesar Ramirez San Juan

Computational Sciences Division

INAOE

©INAOE 2022

All rights reserved

The author grants the INAOE permission for the reproduction
and distribution of this document



To my mother, my father and my closest family.

THANK YOU FOR ALL

Acknowledgments

Mainly, I would like to express gratitude to my advisors, Ph.D. Hayde Peregrina Barreto and Ph.D. Julio César Ramírez San Juan because of all their sincere help, the continuous support, their motivation, all the knowledge that they shared with me, and the quality of the people they are.

The stronger bonds that must be broken are those of the family. It is not easy to be far away; thanks for understanding that.

Sitting at the table is not just for eating. It is to share, grow, regain courage and be happy. Thanks to all my friends at INAOE.

I express my gratitude to all the researchers of INAOE which supported me.

And CONACyT, which helped me with a scholarship.

Abstract

Image processing and analysis acquire and enhance features using mathematical operations over neighboring pixels selected using a predetermined structure with a fixed shape or geometric form. However, fixed analysis windows are not ideal for images with structures of different sizes or shapes, reducing the contrast in the region of interest and thus reducing the image quality as happens in the biomedical field when techniques such as the laser speckle contrast imaging are used. In the medical area, blood vessel visualization is essential for treating and evaluating diseases such as port-wine stains through a contrast image. Although several techniques aim to mitigate the noise level in the contrast images, the visualization of blood vessels is still limited to a superficial location due to its inherent noise. Also, it makes it challenging to select the pixels to compute the contrast value of a region to improve the image quality. The main contribution of this thesis is a method that uses machine learning to select which pixels will be involved in the contrast calculation to compute a contrast representation.

The technique enhances the image quality by selecting the pixels involved in the operation for each pixel using unsupervised learning. Moreover, improving the selection when the analyzed pixel is an outlier value or its neighborhood is composed by noise as happens in laser speckle contrast imaging.

Resumen

El procesamiento y análisis de imágenes consiste en adquirir o mejorar características en una imagen mediante operaciones matemáticas. Las operaciones pueden ser puntuales o extrayendo algún estadístico en una vecindad de píxeles con una forma geométrica fija predeterminada. Sin embargo, las ventanas de análisis fijas no son ideales para imágenes con estructuras de diferentes tamaños o formas. Por tanto, tiende a reducir el contraste en la región de interés, y así, reduciendo la calidad de imágenes. Este efecto de reducción de calidad suele suceder en el campo biomédico al analizar imágenes de moteado de speckle. En el área médica la visualización de vasos sanguíneos es esencial para tratar y evaluar enfermedades como las manchas de vino de Oporto a través del análisis de imágenes de moteado. Aunque varias técnicas apuntan a mitigar el nivel de ruido, la visualización de los vasos sanguíneos aun esta limitada a una profundidad superficial debido al ruido inherente de las imágenes. Además, el ruido limita el uso de técnicas que seleccionen píxeles o ventanas de análisis no cuadradas para realizar un análisis adaptivo.

La principal contribución de esta tesis es el desarrollo de técnicas de procesamiento adaptivo utilizando aprendizaje automático para seleccionar los píxeles que serán considerados para calcular características en cada pixel de la imagen de moteado. La técnica mejora la calidad de la imagen, habilitando el uso de técnicas adaptivas en imágenes con ruido, la cual era la principal limitante de las técnicas adaptivas actuales.

Contents

Acknowledgments	v
Abstract	vii
Resumen	ix
Nomenclature	xxi
Acronyms	xxv
1 Introduction	1
1.1 Problem statement	3
1.2 Research questions	4
1.3 Hypothesis	4
1.4 General objective	4
1.5 Specific objectives	5
1.6 Contribution	5

1.7	Publications resulting from this work	5
1.8	Scope and limitations	6
1.9	Structure of the thesis	7
2	Theoretical framework	9
2.1	Laser speckle contrast imaging	9
2.2	Mathematical Morphology	11
2.2.1	Adaptive mathematical morphology	13
2.3	Image segmentation	16
2.3.1	Supervised learning	16
2.3.2	Unsupervised learning	16
2.4	Image processing techniques	17
2.4.1	Thresholding	17
2.4.2	Evaluation metrics	19
2.4.3	Image normalization	22
3	State of the art	23
3.1	Improvements in the experimental setup	24
3.2	Computational models	29
3.2.1	Traditional methods for contrast calculation	31
3.3	Adaptive processing	34
3.4	Discussion	38

4	Proposed solutions	41
4.1	Adaptive processing by selecting the best size of the analysis window	41
4.2	Adaptive processing by pixel selection	47
4.2.1	Adaptive Threshold Contrast	51
4.2.2	Adaptive Window Contrast	52
4.2.3	Spatially Adaptive Window Contrast	53
4.3	Updating the structuring element	55
4.4	Post-processing step: Morphological filtering of binarized data	56
5	Experiments and results	61
5.1	Data description	61
5.2	Model selection of adaptive window contrast	63
5.3	Experiments by depth	67
5.4	Temporal resolution	74
5.5	Effect of exposure time	76
5.6	Performance of the approaches varying the blood flow	79
5.7	Segmentation results	82
6	Conclusions and future work	85

List of Figures

2.1	RSI of a superficial <i>in-vitro</i> blood vessel.	10
2.2	Contrast representation of a raw speckle image	11
2.3	Example of morphological structural elements	13
2.4	Results of basic operations in mathematical morphology	13
3.1	Sampling volume of light varying the laser wavelength.	25
3.3	Photo-thermal Laser Speckle results.	27
3.5	Motion history image of growing maize seed.	30
3.6	Process to compute a homogeneity representation from a raw speckle image	31
3.7	Traditional approaches to compute a contrast image in laser speckle contrast imaging	33
3.8	Parameters of a elliptical structuring element	36
3.9	Directional analysis used in the anisotropic contrast	37
4.1	Binarization of a raw speckle image	43
4.2	Seed selection in a contrast image image	43

4.3	Regions that grew in blood vessels with different eccentricities	44
4.4	example of a diameter map with two blood vessels obtained after applying the methodology.	46
4.5	Diameter maps obtained in images with bifurcated blood vessels. . . .	46
4.6	Example of an <i>in-vivo</i> contrast image	47
4.7	Representative scatter plot from the static and dynamic regions in laser speckle contrast imaging	49
4.8	Proposed methodology to select the pixels involved in the contrast calculation of each pixel of a raw speckle image	52
4.9	Adjacencies of the analyzed pixels with the cluster centers	54
4.10	Fast adaptive processing of raw speckle images	55
4.11	Histogram of the contrast values in a contrast image	57
4.12	Results of the segmentation improvement for an <i>in-vitro</i> blood vessel at 600μ	59
4.13	Results of the segmentation improvement for an <i>in-vitro</i> blood vessel at 600μ	60
5.1	Experimental setup to acquire raw speckle images	63
5.2	Standardized effects for the statistical model.	64
5.4	Comparison of the contrast images obtained by varying the window size d	66
5.5	Contrast to noise ratio obtained per each depth with the proposed method and the state of the art.	68

5.6	Principal effects of the parameters in the contrast to noise ratio . . .	69
5.7	Qualitative comparisons of the CIs among methods varying the depth.	71
5.8	Comparison of the size maps for the adaptive processing of laser speckle imaging varying the depth and the adaptive method.	73
5.9	Comparison of the contrast to noise ratio obtained varying the frames used to compute the contrast image for the adaptive methods.	74
5.10	Comparison by methods of the contrast to noise ratio obtained by varying the number of frames used to compute the contrast image . .	75
5.11	Comparison of the contrast to noise ratio grouped by methods.	77
5.12	Comparisons of the contrast to noise ratio grouped by methods and exposure time	78
5.14	Comparison of the contrast to noise ratio varying the blood flow . . .	81
5.16	Segmentation comparison between the awK method for feature extraction	84

List of Tables

3.1	Values of Δ_i and Δ_j to establish the neighborhoods at different angles.	31
3.2	Improvement of CIs in the optics area.	39
3.3	Features that can be extracted from a raw speckle image	39
3.4	Contrast methods in the literature.	40
5.1	Parameter values used to perform the model optimization.	64
5.2	Analysis of variance for the full-factorial models.	67
5.3	Multiple comparisons of the results with Tukey and $\alpha = 0.5$	70
5.4	Multiple comparisons for the number of frames used to compute the contrast images	75
5.5	Factors of the experiments.	82

Nomenclature

The next list describes several symbols that will be later used within the body of the document

C_z Set of z clusters.

D Data-set to be grouped.

I_n Normalized image.

I_{max} Upper value to normalize an image.

I_{min} Lower value to normalize an image.

P Probability of a gray scale value to appear in an image.

PC Cost of a path between two data points in an image.

μ_p^W Mean value of an analysis window.

σ_p^W Standard deviation of an analysis window.

cf Cost function to compute a distance between two set of pixels.

dd Data point of a data-set.

$gmax$ Maximum gray scale value in an image.

- $gmin$ Lower gray scale value in an image.
- l Label of an unsupervised algorithm.
- p_0 Central pixel of an analysis window W or S .
- p_i adjacent pixel to p_0
- tr Threshold used in a binarization process.

Contrast Methods

- $aaWK$ Amoeba Adaptive Windowing Contrast
- aK Anisotropic Contrast
- asK Anisotropic Contrast
- awK Adaptive Windowing Contrast
- $sawK$ Spatially Adaptive Windowing Contrast
- sdK Spatial Directional Contrast

Contrast definition

- a Angles to perform an spatial analysis of pixels.
- d Size of the squared analysis window.
- dp Depth at which a blood vessel is located in the RSI .
- K Contrast representation of a image.
- K_p Contrast value of a neighborhood centered at pixel p .
- RI Raw speckle image to be analyzed.
- $stW_p^{d,n}$ Spatio-temporal analysis window centered at p with max size d using n frames.

sW_p^d Squared analysis window centered at p with size d defined in spatially.

tW_p^n Squared analysis window centered at p using n frames.

V Set of pixels obtained with a linear structured element with angles a .

S_p^d Adaptive analysis window centered at p with max size d .

Image definitions

δ Operation performed with a set of pixels selected by a analysis window W or S .

I Color depth (possible values) of an image.

I Input image.

n Number of frames of an image set

p Central pixel of an analysis window.

pp Set of pixels obtained after a δ operation.

Acronyms

aawK Amoeba Adaptive Windowing Contrast. 15, 68, 71–73, 76, 77

aK Anisotropic Contrast. 37, 40, 68–71, 76, 82

ANOVA Analysis of Variance. 68

AP Adaptive Processing. 3

asK Averaged Spatial Contrast. 33, 34, 40, 44, 50, 58, 63, 64, 68, 70, 71, 75, 76, 82

awK Adaptive Window Contrast. 41, 52, 61, 64, 68–73, 75–77, 79, 80, 82, 85

BF Blood Flow. 1, 23, 24

CA Classical Analysis. 2, 5

CI Contrast Image. 2–4, 7, 10, 11, 20, 21, 23–25, 28, 32, 33, 36–39, 42, 44, 45,
47–49, 56–59, 61, 67, 68, 70, 71, 74–76, 78, 79, 85, 86

CNR Contrast to Noise Ratio. 21, 22, 63, 64, 66, 68, 69, 74–78, 80, 85

COM Co-Occurrence Matrix. 30, 31, 39

EASE Elliptical Adaptive Structuring Element. 35

F1 F_1 Score. 20

FN False Negatives. 19

FP False Positives. 19

JI Jaccard Index. 20

LSCI Laser Speckle Contrast Imaging. 1, 2, 4, 5, 7, 9, 10, 21, 23–25, 29, 31, 32, 36, 38, 39, 41, 44, 47, 59, 67, 79, 85

LSI Laser Speckle Imaging. 42

MA Morphological Amoeba. 34, 35

MESI Multi-Exposure Time Laser Speckle. 25, 26

MHI Motion History Image. 29

MM Mathematical Morphology. 12

MMLS Magneto Motive Laser Speckle. 26

MN Micro Needling. 26

msK Multi Scale Contrast. 36, 40

MV Microvasculature Visualization. 1, 23

PCTOC Physico Chemical Tissue Optical Clearing. 26

PTLS Photo-Thermal Laser Speckle. 25, 27

RBF Relative Blood Flow. 1, 9

ROI Region Of Interest. 11, 26, 42, 47, 56, 59, 70, 72

RSI Raw Speckle Image. 2–5, 7, 10, 11, 15, 24, 25, 29–33, 36–40, 42, 43, 47–50, 57, 58, 62, 63, 86

sawK Spatially Adaptive Windowing Contrast. 41, 68, 69, 71–73, 75–77, 79, 82, 85

sdK Space Directional Contrast. 37, 40, 68–72, 76, 80, 82

SE Structuring Element. 12

SFI Speckle Flow Index. 27

sK Spatial Contrast. 32–34, 40

stK Spatial Temporal Contrast. 34, 40

tK Temporal Contrast. 33, 34, 40, 63, 64

TN True Negatives. 19

TNR True Negative Rate. 19, 20

TP True Positives. 19

TPR True Positive Rate. 19, 20

TSK Three Sizes Contrast. 36

Chapter 1

Introduction

Blood flow is considered necessary for the physiological functions of the body. The efficient functioning of the human body is dependent on good blood flow.. If the blood flow is affected by an illness, the cardiovascular functions and the microvasculature can be affected. Thus, it is essential to visualize the microvasculature and the blood flow in the medical field. Microvasculature Visualization (MV) is concerned with identifying blood vessels in biomedical images, and currently, computational algorithms can help to visualize them with more precision.

Due to the importance of MV and the study of the Blood Flow (BF), several techniques have been developed to visualize and measure them, such as the doppler fluxometry [1, 2], optical computer tomography [3], or the magnetic resonance [4, 5]. In contrast, the Laser Speckle Contrast Imaging (LSCI) is a cheaper technique, non-invasive that allows the visualization of the smaller blood vessels. For these reasons and its simple instrumentation, it is widely used because of its advantages over the traditional methods to MV.

LSCI has several applications in the medical field due to its improved spatial and temporal resolution to MV. It is helpful to measure the Relative Blood Flow

(RBF) [6] in the evaluation and treatment of certain diseases such as the Port-wine stain, photo-dynamic therapy [7]. Also, it can be used to visualize and analyze obstructed blood vessels [8], or to estimate the diameter of blood vessels to track diseases such as diabetes, hypertension, or retinopathy [9, 10, 11]. Among other applications, LSCI additionally can be used to visualize the cerebral activation of specific regions in the neurological field [4].

The LSCI technique captures the movement of blood flow particles during a period of time through a set of images [12, 13]. Since the particles in the blood flow move faster, a momentum transfer phenomenon accelerates the oscillation of speckles in the captured images, generating a blurring pattern when the camera integrates the image. Thus, the blurring in a Raw Speckle Image (RSI) can be associated with blood flow, meanwhile a random interference pattern of dark and bright speckles to its absence [8]. Providing a way to associate the movement in a tissue blurring pattern with blood flow movement in areas with microvasculature [14, 15]. Such information can also be used to locate and analyze blood vessels using a Classical Analysis (CA) departing from the RSI.

Since the tissue between the camera and the imaged blood vessels disperses the light, it generates a high level of noise in the image, making it difficult to visualize the periphery where the blood vessel is located. Then, the visualization of blood vessels with LSCI is restricted to superficial microvasculature, i.e., a depth $< 300\mu m$ [16] since the structures adjacent to the blood vessel produce high dispersion of photons due to optical scattering [17]. Aiming to alleviate the noise and depth problem in LSCI, several approaches to perform the CA was proposed where a squared or linear neighborhood around the analyzed pixel contains the pixels involved in the contrast calculation, but the use of the CA is a trade-off between contrast among regions, noise, spatial and temporal resolution because it is difficult to identify between regions in Contrast Image (CI), s in which the deep of the blood vessels is not superficial. Thus, to improve the image quality of CIs, several

anisotropic approaches have been proposed to calculate the statistics using a subset of the traditional selection in the squared neighborhood. Although there is an improvement in the image quality, the anisotropic methods introduce artifacts in the image because the pixel selection is not ideal [18]. After all, they are still using a fixed neighborhood. On the other hand, if state-of-the-art methods for Adaptive Processing (AP) select the pixels involved in the contrast calculation for each pixel in the RSI, the morphology of the structure formed by the chosen pixels does not fit with the real one. The pixel selection in the RSI is not a trivial task because of the inherent noise in it. Commonly the outlier values are isolated, or the pixel selection is not representative of the analyzed pixel.

Some works have addressed blood vessel location at depths $> 300\mu m$, but they often require a physical change of the technique which can be invasive and inadequate in sensitive areas such as retina or brain [19, 20, 21, 22]. Other works are focused on noise attenuation establishing different ways of speckle correlation (spatial, temporal, and space-temporal), for contrast calculation [16, 23]. However, the main drawback is related to the compromise between noise attenuation and temporal resolution. Also, some contrast approaches differ in the way they select the pixels for contrast calculation, i.e., it may be considering an isotropic or anisotropic window [24] and also differ in the use of a fixed size or a size-adapted window [25].

1.1 Problem statement

We aim to improve the quality of the CIs to segment the blood vessels at depths $300 \mu m > dp < 1000 \mu m$. We look to compute a feature δ more representative to the analyzed neighboring. The computational model is $m(f(RI, \{\delta_1, \delta_2, \dots, \delta_n\})) = I_s \in \{0, 1\}$. Where $RI^{(b,t,d)} = \{ri_1, ri_2, \dots, ri_n\}$ is a set of n RSIs of b bits with values between $[0, 2^b]$, exposure time t , a depth d in the range $[0, 1000] \mu m$, δ is a function that compute a feature from a set of values, I_s a segmented image with markers where

0 indicates that the pixel is not considered a blood vessel and 1 indicates the regions of interest, f is the adaptive processing of the RI to compute δ_n (contribution) and m a classification model.

1.2 Research questions

The main research questions that motivated this thesis are:

- How a contrast representation can be improved by using adaptive image processing techniques?
- How much the image quality of CIs can be improved by using the proposed method?
- How much the location of blood vessels in CIs will be improved by using the proposed method?

1.3 Hypothesis

If instead of using the pixels in a squared neighborhood, they are selected to compute a representation, the spatial variations in them can be reduced, improving the visualization of blood vessels in LSCI images.

1.4 General objective

To segment blood vessels in RSIs using a set of features computed by the proposed method which selects the involved pixels in its calculation for each pixel in the image.

1.5 Specific objectives

1. To develop an adaptive image processing technique to perform the CA of a RSI to improve its quality.
2. To develop an adaptive image processing technique to extract features from a RSI and apply a classification algorithm to obtain a segmented image I_s with markers that approximate I_{gt} .
3. To validate the proposed adaptive contrast calculation.
4. To validate the proposed adaptive feature extraction method.

1.6 Contribution

As a result of this thesis, a method to adaptively process a RSI will be delivered. Then, the contributions of this work are:

- A method to select the pixels used to compute a contrast representation in LSCI. The criterion must be robust to high spatial variations since it is a common property of the images in the domain.
- A segmentation scheme to adaptively obtain the features used to train a classification algorithm.

1.7 Publications resulting from this work

- JCR Journal papers

- Adaptive processing for noise attenuation in laser speckle contrast imaging, *Computer Methods, and Programs in Biomedicine*, Volume 212, 2021, 106486, ISSN 0169-2607.
- Conference papers
 - A morphological approach for locating blood vessels in laser contrast speckle imaging, 2018 IEEE International Instrumentation and Measurement Technology Conference (I2MTC), 2018.
 - Estimation of blood vessels diameter by region growing in laser speckle contrast imaging, 2019 IEEE International Instrumentation and Measurement Technology Conference (I2MTC), 2019.
- Poster presentation of early results
 - Improvement of blood vessel visualization in laser speckle contrast imaging using adaptive processing methods, 2021, XI Congreso nacional & I congreso internacional de tecnología aplicada a ciencias de la salud, Facultad de medicina UNAM, México.
 - Effect of exposure time in adaptive processing of Laser Speckle Contrast Imaging, 2021, IEEE-EMBS International conference on biomedical and health informatics, virtual conference.

1.8 Scope and limitations

Image processing and analysis acquire and enhance features using mathematical operations over neighboring pixels selected using predetermined windows with a fixed shape or geometric form. However, fixed analysis windows are not ideal for images with structures of different sizes or shapes, for example, reducing the contrast in the

region. This research aims to improve the algorithm to compute the contrast representation of CIs in LSCI. The identification of blood vessel depth is not addressed in this work. Analysis in the frequency domain and modification to the experimental setup for RSIs acquisition is out of the scope of this thesis.

1.9 Structure of the thesis

This chapter briefly introduces the motivation of the work along with a general overview of the thesis emphasizing the research questions, the hypothesis, and the objectives that guided this dissertation. Chapter 2 presents the underlying theory necessary to understand the methods in this thesis. Chapter 3 briefly discusses the literature to understand how current research addresses the problems of noise and low contrast in LSCI. Chapter 4 describes the steps toward the development of the adaptive methods proposed in the dissertation. Chapter 5 reports the experiments performed towards the validation of the proposed techniques. Each subsection describes the rationale of the experiment and the results obtained. The qualitative and quantitative results were reported along with the statistical analysis required to validate the results. Finally, in Chapter 6, the conclusions of this research and suggested future work are discussed.

Chapter 2

Theoretical framework

This chapter introduces the basic concepts used to understand the development of this dissertation. The first section describes the application domain, the LSCI technique is described as well as the contrast representation used as the main feature to identify blood vessels. Later, image processing techniques are defined to understand the process of semantic classification. The described methods initiate from the mathematical morphology until image segmentation definition.

2.1 Laser speckle contrast imaging

Several techniques have been developed in the optical area due to the importance of visualizing microvasculature and measure its blood flow. Although is essential to evaluate and treat some diseases in the medical field by analyzing blood flow, it is important to do it through non expensive and non invasive techniques. Among the techniques to measure RBF, LSCI is widely studied due to its improved spatial resolution and low cost.

LSCI is useful to visualize microvasculature by analyzing the movement of the

blood flow through an optical phenomenon called laser speckle. When coherent light illuminates an object, the reflected and scattered waves produce a random granular effect known as speckle. When a camera captures the scattered light from an object with an exposure time higher than the shorter speckle fluctuation, a RSI is obtained (Fig. 2.1) [16, 15]. The RSIs consist of bright and dark pixels that result from the interference of the individual light waves that reach each detector of the camera sensor and if the scattering particles are in motion, the speckles fluctuate faster than particles without movement due to momentum transfer [13] forming two types of patterns. In the static region, a noisy pattern with high contrast between speckles is formed and in the region with movement, a blurred pattern is formed due to the faster speckle fluctuations.

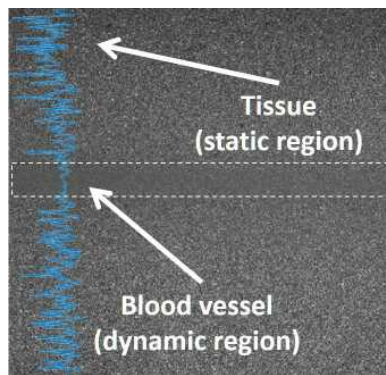


Figure 2.1: RSI of a superficial *in-vitro* blood vessel, the blue profile is related to the intensity variations in the static and dynamic regions.

Thus, if a pattern with high gray levels variations in the RSIs perceived as a noisy region is associated with particles with low movement, and moving particles are associated with a blurred area, the regions can be used to analyze blood flow behavior. The particle movement in LSCI can be studied using contrast values computed from a RSI, the obtained image is called a CI (Fig. 2.2). A process repeated pixel by pixel of the RSI computes the local contrast value K_p using the standard deviation σ and the mean intensity μ of a sliding window W_p centered at its central pixel p using the Eq. 2.1.

$$K_p = \frac{\sigma^{W_p}}{\mu^{W_p}} \quad (2.1)$$

In ideal conditions, the σ and μ values of an RSI are equal [16] but σ tends to decrease when particle movement is present in the sensed object, indicating similitude among the gray values, and then K approximates 0; otherwise, K obtains values near 1. Thus, intensity values in a RSI measured through contrast values in a CI, are associated with homogeneous and noisier regions, respectively.

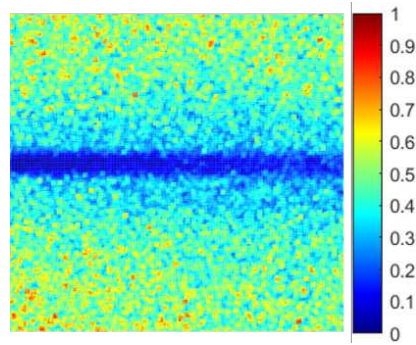


Figure 2.2: Contrast representation or CI computed with a window of 5×5 of Fig. 2.1. Low values (blue) are related to blood vessels and high values (red) with static tissue.

2.2 Mathematical Morphology

A digital image can be considered a discrete matrix with square elements known as pixels, where pixels are the sampling spots from a sensor. Each value represents the photons sampled at a specific point. Two basic types of images are discussed in this section, binary and gray-scale images. In the binary case, the pixels can only take two values, thus, they are those that can take values where $p \in \mathbb{R}[0, 1]$ for simplicity; a 0 value represents a background region, and a 1 value as the Region Of Interest (ROI). In the other case, we will consider a matrix limited by the color depth b as a gray-scale image as 2^b . The color depth defines the number of values that I can

take. In this research, the images have a color depth of 8 bits, which means images are limited to $2^8 = 256$ possible values.

The Mathematical Morphology (MM) defines an analysis theory of binary and gray-scale images based on the shape of objects present in them. The MM describe its operations by using set theory, integral geometry, and lattice algebra [26, 27]. Thus, the basic operations of MM are defined with unions, intersections, or set complements for image filtering, segmentation, or shape comparison. Being the Structuring Element (SE) or convolution matrix essential to process an image, they are used [28]. Morphological operations can be defined using functional notation or using operation symbols [18].

$$\Psi S(I) = I\Psi S \quad (2.2)$$

where the morphological operation such as noise attenuation filter, or shape probe is defined as δ , operating in the image I using the structuring element or convolution matrix S . Where S is commonly a rigid structuring element composed of the 0 and 1 values that probe the image for each data-point in I . The SE is used to extract relevant information probing the image; In most cases, the geometric shape is defined or selected according to prior knowledge about the relevant or irrelevant information in the analyzed image. On the other hand, in adaptive mathematical morphology, it can change accordingly to the information of a neighboring of the probed pixel and it also can be used to select the pixels involved in the δ operation. Fig. 2.3 shows some rigid basic structuring elements.

MM uses two basic operations from which its combination can lead to more advanced processes for binary and gray-scale images, each type of image have its particular processes to probe the image. In the binary case of the morphological operations, the erosion denoted as $I \ominus S$ reduces the image I using a binary structuring element S translated to a pixel p (S_p), maintaining the pixels that belong to I and



Figure 2.3: Two types of structural elements (a) squared structural element (b) structural element of type disk.

S_x when its origins converge and discarding those that do not fulfill the condition. On the other hand, the dilation of an image adds pixels to the original image. It contains the location of the pixels where the structuring element S_x hits the image I , expanding it. Fig. 2.4 depicts the results of erosion and dilation of a binary image with a blood vessel in it.

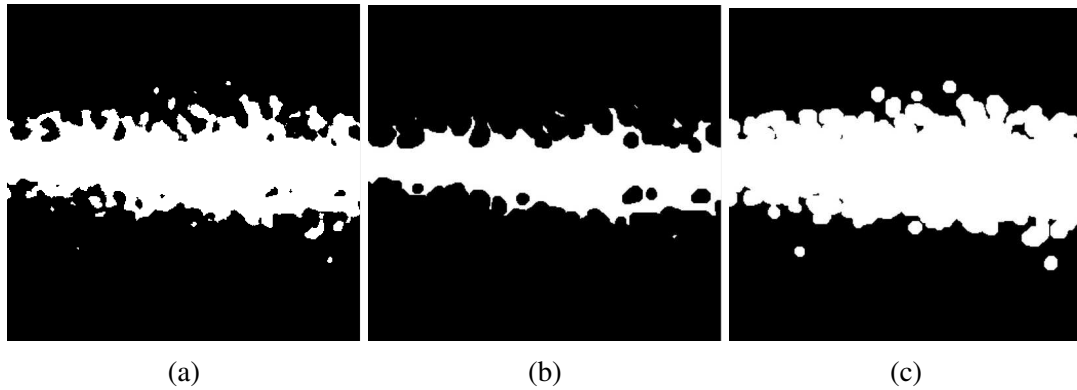


Figure 2.4: Basic operations of mathematical morphology (a) binarized image of a blood vessel (b) erosion of Fig. 2.4a, and (c) dilation

2.2.1 Adaptive mathematical morphology

Some operations in image processing and analysis such as filtering, feature extraction, segmentation, or shape comparison in I must select the pixels involved in such process by using a matrix S . Thus, S is a mask that indicates which pixels of the

neighborhood are involved in an operation Ψ over I [26, 29]. Traditional methods define the matrix S for pixel selection with a fixed shape or size to process the whole image. Although a fixed S is efficient, it loses valuable information if the ROIs in the image differ in shape or size [29]. In adaptive image processing, the characteristics of S_p (size and shape) may vary for each pixel according to the neighboring of p and a given criterion. Thus, the adaptive processing methods process each pixel p with a S_p computed in the neighborhood around p with a maximum size d . Therefore, a S_p is defined for each p in I to apply δ aiming to preserve the information of its similar pixels. Thus, let S_p^d be the convolution matrix superimposed over the central pixel p with a maximum window size d to adjacent pixels in the directions $\theta = \{0^\circ, 45^\circ, \dots, 180^\circ\}$, containing the values $\{0, 1\}$ where 1 indicates the pixels that will be used in the δ transformation. Values in S_p^d are determined by comparing the central pixel p_0 of the neighborhood with its underlying pixels using a similarity measure (euclidean, geodesic, or a composed distance) and marked as 0 or 1 according to a given criterion [30]. Standard techniques use a region growing process considering the distance between the mean value of the pixels marked as 1 ($pp \in S_p^r | pp = 1$) and their adjacent pixels (p_i) where p_0 is the only element marked as 0 at the first iteration. Then, the pixels p_i that fulfill a threshold t are set to 1, increasing the initial region area (seed) composed only by p_0 (Eq. 2.3). Equation 2.3 summarizes the construction of the analysis window [31, 32]. In the state of the art methods, if p_i or p_0 is an outlier value, the selection of S_p could be inaccurate. A smoothed version or feature map of RI is used to attack the outliers problem, known as the reference image R to improve the pixel selection since noise is attenuated in R [33, 18]. The basic algorithm for adaptive processing is depicted in Algorithm 1 [28].

$$S_p^d(p_i) = \begin{cases} 1, & \sqrt{[\mu^{S_p^d} - I(p_i)]^2} < tr \\ 0, & \text{otherwise} \end{cases} \quad (2.3)$$

Algorithm 1 General algorithm for adaptive processing

Require: I, d

Ensure: Output image O

- 1: **procedure** ADAPTIVE PROCESSING(I, r)
 - 2: compute R from I
 - 3: **for each** pixel $p \in I$ **do**
 - 4: compute S_p^d using R
 - 5: $O_p \leftarrow I \delta S_p^d$
 - 6: **end for**
 - 7: **end procedure**
-

Morphological amoeba

The morphological amoeba aims to establish a connected set of pixels to operate Ψ . The morphological amoeba selects the pixels using a geodesic distance at a max distance r computed from p_0 to each p_i in a squared neighborhood. The included pixels in S are those with a distance less than r . Thus, let $PT(x, y) = \{x_1, \dots, \dots x_i, x_{i+1}\}$ be a path connecting points between pixels x and y . The cost of the path is $PC(x, y) = PT(x, y) \sum_{i=1}^{n-1} cf(x_i, x_{i+1})$. The selected pixels pp to compute δ are $S_p^r = \{pp \in R : \min PC(x, y) < r\}$. where r is a parameter to determine the size of S and cf is a cost function:

$$PC(p_i, p_{i+1}) = 1 + \Delta |R(p_i) - R(x_{p+1})| \quad (2.4)$$

R is the reference image which is commonly a feature map such as an edge or salience filtered version of I . It is used to reduce the impact of the noise in the pixel selection. The modification to compute the contrast representation of an RSI is going to be called the Amoeba Adaptive Windowing Contrast (aawK) for simplicity.

2.3 Image segmentation

Classification in computer sciences is the task to assign a class label to an observation in a data set based on statistical analysis. In image classification, observations can be all the pixels that represent an image, and in this particular case, the process is called image segmentation. When the observations are classified into Z groups with prior awareness of whether an observation belongs to a class c_1 or c_2 it is called supervised learning; otherwise, it is called unsupervised learning.

2.3.1 Supervised learning

Given a set of n data points, also called observations, $D = \{ \langle f_1, c_1 \rangle, \langle f_2, c_2 \rangle, \dots, \langle f_n, c_n \rangle = \langle F, C \rangle \}$. Where f can be a multidimensional vector of the form $f_i = \{f_1, f_2, \dots, f_n\}$ and c_i the class or label of the observation f_i . f_n is a set of features obtained through feature extraction functions $\{\delta_1, \delta_2, \dots, \delta_n\}$. The features can be i.e. statistics measures from a set of pixels in a $d \times d$ neighborhood defined by an analysis window W^d for a squared fixed shape or $S^d \subseteq W^d$ for an adaptive selection of pixels. The pixels involved in the calculation of f_n may be based on the local information of W^d . Thus, the goal of a classification process is to infer an unknown function or relation m between the features f_i and a class c_i represented as $c = m(f)$ such that $m(f) : F \rightarrow C$ [34].

2.3.2 Unsupervised learning

Unsupervised learning is a technique that consists of grouping data according to a given criterion. The most known algorithm is Lloyd's algorithm, which aims to minimize the distance between a set of data points in a cluster $dd \in c$. [35]. The algorithm focuses on choosing c centers $C = \{c_1, \dots, c_z\}$ that minimize Eq. 2.5.

Algorithm 2 Lloyd's algorithm

Require: D, z **Ensure:** centers C

- 1: Random choosing of z initial centers $c \in D$
 - 2: **repeat**
 - 3: **for each** $dd \in D$ **do**
 - 4: Find the nearest center $c(dd)|c \in C$
 - 5: **end for**
 - 6: **for each** $c \in C$ **do**
 - 7: $c \leftarrow \sum_{\{dd \in D | c(dd)=c\}} \frac{1}{|c|} dd$
 - 8: **end for**
 - 9: **until** $|C_i| = |C_{(i-1)}|$
-

$$\Theta = \sum_{dd \in D} \min_{c \in C} \|dd - c\|^2 \quad (2.5)$$

The algorithm begins with a random choice of z centers c . Then, each data point dd is assigned to its nearest center c . The centers are recomputed based on the mean of the data points assigned to them. As shown in Algorithm 2.

2.4 Image processing techniques

Several image processing techniques will be presented to define the processes that can be used to improve the quality of the feature representations in terms of noise and spatial resolution. Thus, the next section will introduce the techniques used for pre-processing or post-processing the analyzed images.

2.4.1 Thresholding

To binarize an image is related to assigning a label to each pixel of the image I based on a criterion. Some criteria can be a similarity measure or a threshold that groups

regions with the same gray values. For example, thresholding can segment an image into two sections, the background and the region of interest, assigning them a 0 and a 1, respectively. The process of labeling based on a threshold tr can also be named binarization and can be defined with the following equation:

$$I_{bw}(x, y) = \begin{cases} 1, & \text{if } (x, y) \leq tr \\ 0, & \text{otherwise} \end{cases} \quad (2.6)$$

The main drawback of binarization is selecting the correct tr to separate the ROI properly from the background. The most used algorithm is the Otsu method, which allows estimating tr by analyzing cumulative moments of an individual image. This method assumes a bimodal distribution where there are only two main regions in the image, such as the background and the ROI (or the static and dynamic regions in CI), searching the maximum variance of class separability, defined as:

$$\sigma_B^2(tr) = \frac{(\mu T \cdot \omega(tr) - \mu(tr))^2}{\omega(k)(1 - \omega(tr))} \quad (2.7)$$

$$\omega(tr) = \sum_{l=1}^t r_{l=1} P(l)$$

$$\mu(tr) = \sum_{l=1}^t r_{l=1} l \cdot P(l)$$

$$\mu T = \sum_{l=1}^{N_{max}} l \cdot P(l)$$

where k is the current analyzed gray value, and N_{max} is the maximum gray level to consider (255 for a 8-bits image) [36] and $P(l) = |\{p \in I | I_p = l\}|$.

2.4.2 Evaluation metrics

Several evaluation metrics can be used to measure the performance of algorithms. In this section, a set of evaluation metrics are briefly described; the presented methods focus on segmentation metrics to assess the correctness of the separability of the regions and metrics to evaluate the quality of the image as contrast or noise.

Segmentation metrics

Before defining any metric, it is imperative to know the meaning of True Positives (TP), True Negatives (TN), False Positives (FP) and False Negatives (FN). Given two binary images A and B composed by the values 0 and 1 where 1 is the object and 0 is the background, $TP = |A \cap B|$, $TN = |A^c \cap B^c|$, $FN = |A \cap B^c|$ and $FP = |A^c \cap B|$.

Accuracy (ACC) or the ratio of correctly segmented pixels over all pixels (for this domain) can be calculated using the following equation:

$$ACC = \frac{TP + TN}{TP + TN + FP + FN} \quad (2.8)$$

The sensitivity or True Positive Rate (TPR) measure the proportion of pixels correctly segmented is defined as follows:

$$TPR = \frac{TP}{TP + FN} \quad (2.9)$$

Specificity or True Negative Rate (TNR), measure the proportion of background pixels that are correctly identified as such and is defined with the following equation:

$$TNR = \frac{TP}{TP + FP} \quad (2.10)$$

F_1 Score (F1) is a metric used to evaluate classification results, this metric, can be extended to evaluate image segmentation. F1 is the harmonic mean of TPR and TNR:

$$F1 = \frac{2TP}{2TP + FN + FP} \quad (2.11)$$

Jaccard Index

Although it is the most used metric, accuracy does not provide enough information about over-segmentation and infra-segmentation. In the case of the LSCI images, the CIs are composed mainly of background areas, which can lead to a misinterpretation of the results. To address this issue, the Jaccard Index (JI) is used as the main evaluation metric.

JI is a similarity coefficient between two sets A and B , defined as $JI(A, B) = \frac{A \cap B}{A \cup B}$, that basically is their intersection over their union. JI is a coefficient that denotes how much two sets are similar. JI result is in the range $[0,1]$ where a 0 denotes a lack of similarity and 1 means that the segmentation contains a perfect match. For particular purposes in images, JI can be used as an overlap coefficient between two binary images, thus, the JI is defined as:

$$JI(Is, Igt) = \frac{Is \cap Igt}{Is \cup Igt} = \frac{TP}{TP + FP + FN} \quad (2.12)$$

where Is is the segmented image and Igt is related to the ground truth image.

Contrast-to-Noise Ratio

The Contrast to Noise Ratio (CNR) is a measure commonly used by different LSCI approaches to evaluate image quality [37, 4, 17, 38]. It provides a way to measure the contrast between the static and dynamic regions of an LSCI image by the difference of their means ($\mu_{dynamic}$, μ_{static}) penalized with the standard deviation of the static region (σ_{static}). Thus, higher CNR values are associated with improved visualization of the blood vessels in terms of noise attenuation and higher contrast between static and dynamic regions.

Although the CNR value provides a quality measure of the improvement reached in the CI most of the area in CI corresponds to the static region while the total area of the dynamic region is significantly smaller. Therefore, when statistics are calculated to compute CNR, the mean contrast value is mainly influenced by the static region. If the CNR measure is obtained from dynamic and static patches, the high difference of values increases the contrast mean, indicating a high contrast between regions although the improvement may not be visually perceptible. Consequently, a more fair comparison to indicate better visual discrimination could be made by taking patches from adjacent regions, i.e., the dynamic and transition regions (Figs. 4.7d-4.7d).

The transition region in LSCI consists of a mix of detected photons that interact with static and dynamic scatters; consequently, the contrast values have different behavior, they do not vary as much as in the dynamic regions, nor are as similar as in the static region. To overcome this inconsistency in the measurement, it is proposed to take into account the difference between pixels at a distance t from the periphery of the static region and pixels from the dynamic region. Thus, it is ensured that the CNR value is measuring the improvement in the region of interest.

The periphery and dynamic regions were identified by using a predefined mask (Fig. 2.5a) that depicts the regions involved in the CNR calculation. Statistics

from the dynamic region are computed from the pixels in green, and compared with the statistics from the periphery in red; the difference is obtained between pairs of corresponding points (Fig. 2.5b). In this way, it is expected that the CNR be consistent with the perceived visual improvement using the Eq. 2.13.

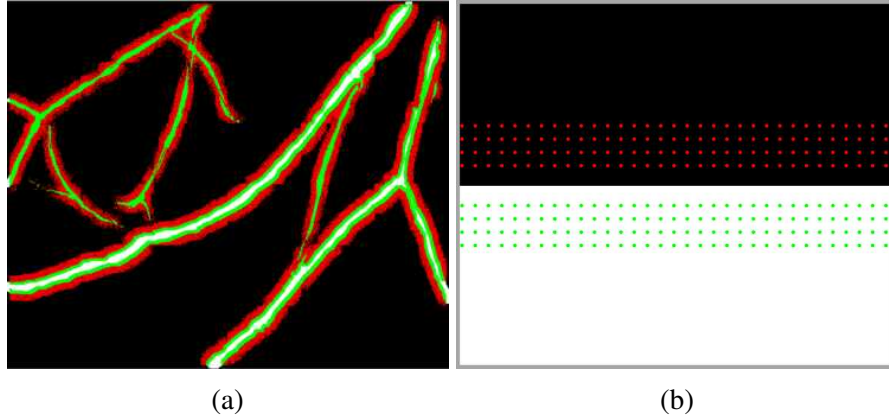


Figure 2.5: Proposed selection of pixels from the edge of the blood vessel to compute the CNR; in green the selected pixels from the blood vessels and in red pixels from the tissue. a) An overview of a *in-vivo* image and b) A close-up of a blood vessel depicting the selected pixels.

$$CNR = \frac{|\mu_{dynamic} - \mu_{static}|}{\sigma_{static}^2} \quad (2.13)$$

2.4.3 Image normalization

Image normalization is used to stretch the range of intensity values by scaling them into a new range $[g_{max}, g_{min}]$ given by a max value g_{max} and a min value g_{min} [36]:

$$In(x, y) = \frac{g_{max} - g_{min}}{I_{max} - I_{min}}(I(x, y) - I_{min}) + g_{min} \quad (2.14)$$

Where In represents a normalized pixel of the image I and I_{max} and I_{min} are the maximum and minimum values, respectively.

Chapter 3

State of the art

MV and BF analysis in tissue are parameters widely used in medical areas such as dermatology, ophthalmology, and neurosciences because of their several applications in the biomedical field [6, 39]. Due to the importance of MV, several techniques have been developed to improve the visualization of blood vessels in tissue, such as doppler flowmetry [40, 2], multiphoton tomography [41, 42], magnetic resonance [4, 5] and computer tomography [3]. However, these techniques have higher monetary cost, leading to research into simpler and affordable image techniques. On the other hand, LSCI is a low cost non-invasive technique with simple instrumentation that allows visualization of the thin blood vessels in tissue, and with greater spatial and temporal resolution. Nevertheless, LSCI is restricted to superficial microvasculature, i.e., depth $< 300 \mu\text{m}$ [16, 43], since structures adjacent to blood vessels produce high dispersion of photons due to optical scattering [13]. The main limitation concerning the visualization of blood vessels in LSCI is observed when blood vessels are present at depths $> 300 \mu\text{m}$. Deep blood vessels in LSCI have a less spatial resolution because their periphery contains high quantities of noise, making it challenging to measure its diameter and identify its periphery [12]. Several techniques for noise reduction in the CI or segment blood vessels in CI have been proposed, but there is still room

for improvement. In this section, the efforts reported to improve the visualization of depth blood vessels are discussed.

3.1 Improvements in the experimental setup

Some techniques aim to improve the visualization of the blood vessels in LSCI in the optics area by modifying the characteristics of the experimental setup (Sec. 5.1). For example, the experimental setup can be modified to improve the conditions in which the RSIs are imaged by changing the laser, exposure time, focal length of the camera, or by introducing external agents in the BF torrent to improve its dynamics. In the optics area, several works aim to improve the quality of the CI by searching for a laser that improves the sampling volume in the tissue [44]. A suitable laser selection enables the best penetration of the photons to sense the information adequately in the tissue at high depths. The sampling volume is the quantity of information that a laser is capable to recollect in tissue and with the capabilities of the light to penetrate tissue. For instance, the 632.8 nm laser used for the *in-vitro* samples (Sec. 5.1) ensures a light penetration of $\approx 1500 \mu\text{m}$, comprising the maximum depth used in the experiments performed in this thesis ($900 \mu\text{m}$) (Fig. 3.1) [45].

The exposure time during the acquisition of RSIs is the timelapse it takes for the camera to capture the scattered and reflected light from the imaged tissue. It plays an essential role in the quality of the image. If the exposure time is longer than the correlation time of the scattered light, the blurring pattern in the dynamic region increases, providing better visualization of blood vessels. Nevertheless, the main drawback of increasing the CCD camera exposure time is the reduction of temporal resolution and the impossibility of imaging tissue in motion. Thus, to select a suitable exposure time is necessary to generate RSI with a suitable relation between image quality and temporal resolution with respect to previous techniques. In recent works, there are experiments to select a proper exposure time for a specific

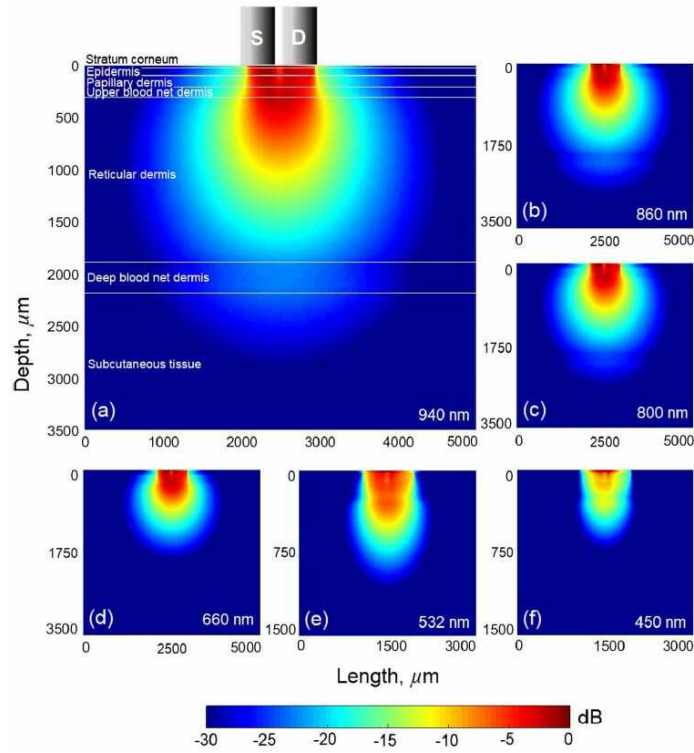


Figure 3.1: Sampling volume of light with (a) 940 nm, (b) 680 nm, (c) 800 nm, (d) 660 nm, (e) 532 nm and (f) 450 nm. Fig. taken from [45].

method to optimize the visualization of blood vessels. Also, works where a Multi-Exposure Time Laser Speckle (MESI) is performed, optimizing the exposure time for a certain set of images, as depicted in Fig. 3.2. Thus, it is important to select the proper exposure time to allow LSCI to have online applications, including sensing areas with micro-movements such as eyes or images in children. [46, 22, 47, 48].

Some works found that introducing external agents to generate movement in the blood flow torrent can improve the contrast between the static and dynamic regions in CIs enhancing the dynamics of the blood flow in different ways [49]. For example, Photo-Thermal Laser Speckle (PTLS) radiates the tissue with laser light, exciting and heating the blood that circulates through the blood. Then, the heated blood flow increases particle movement inside the blood vessels that later is captured by the LSCI technique, increasing the blurring effect contrast in the RSI [50]. On the

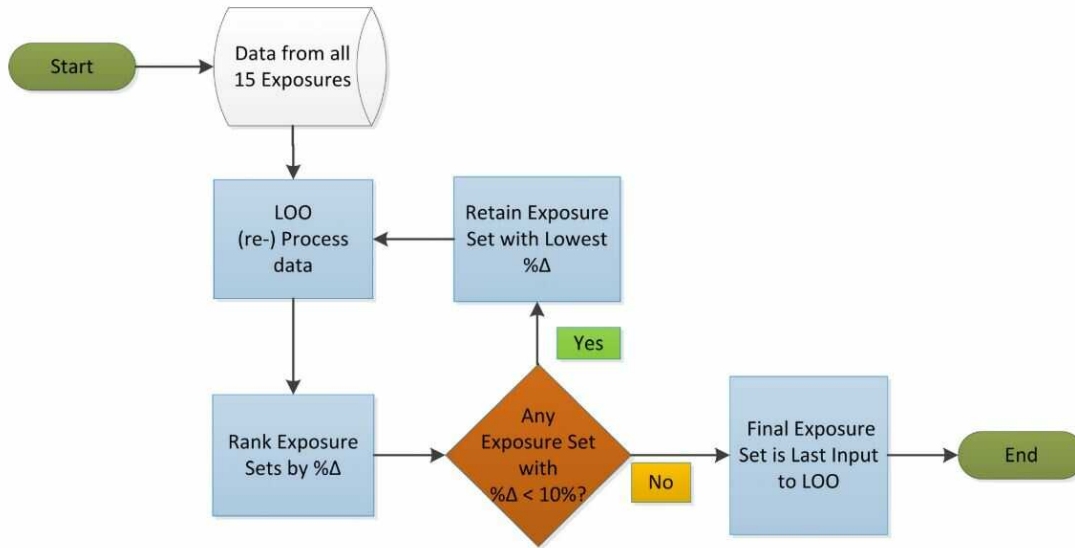


Figure 3.2: Optimization of the exposure time, the protocol is designed to rank and select the best exposure times in MESI. Diagram taken from [47].

other hand, Magneto Motive Laser Speckle (MMLS) introduces iron oxide particles in the blood flow torrent to later excite them with a solenoid coil generating movement in the blood flow torrent, causing an improvement in the blurring of the dynamic region. [20].

As mentioned before, the scatter tissue surrounding the imaged vessel, which increases as its depth does, is the main limitation of the optical methods. Thus, techniques such as the Micro Needling (MN) or Physico Chemical Tissue Optical Clearing (PCTOC) tackle the limitation of the scattering tissue to improve the loss of spatial resolution caused by the mixed pixels of sensed photons that interacted with the two main types of tissue. The PCTOC technique combines the MN method with a topical application of glycerol to prepare the sensed tissue to enhance the contrast of LSCI. First, a microneedle-roller was used 50 times in three directions (horizontal, vertical, and diagonal) to create microchannels in the skin to deliver the glycerol. Then, a glycerol concentration at 70% was applied in the ROI. As a result, the MN and the PCTOC method enhanced the light penetration and therefore reduced the

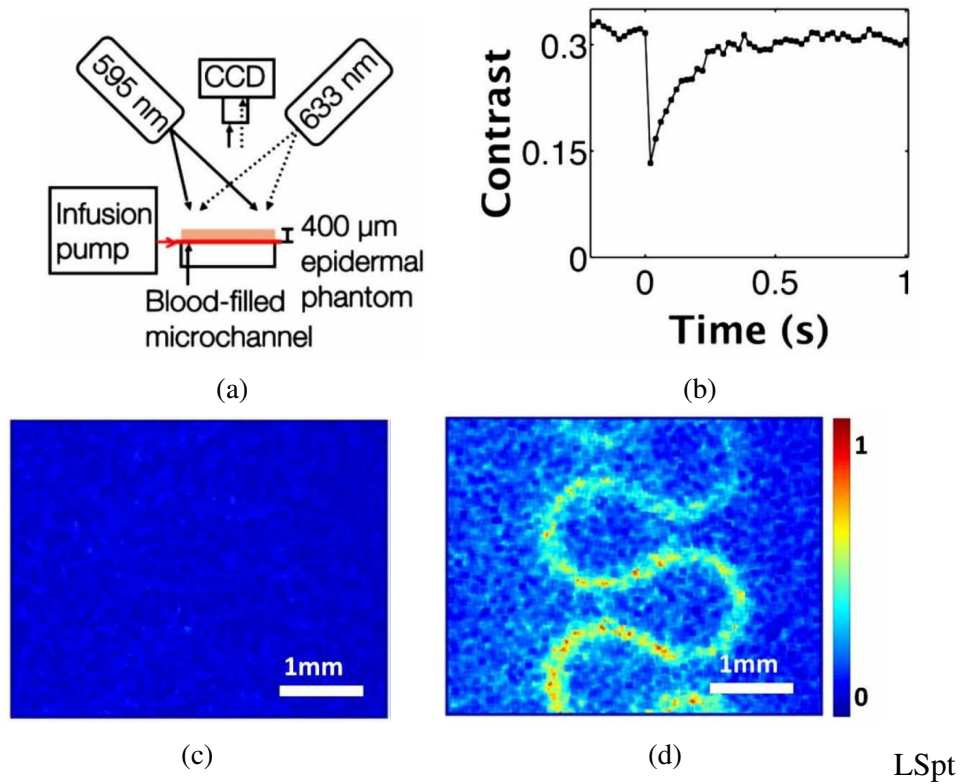


Figure 3.3: PTLS of a simulated blood vessel infused at 4 mm/s in a 400 μm phantom above the micro-channel. a) Experimental setup, b) Speckle contrast, c) normalized Speckle Flow Index (SFI) before excitation and d) normalized SFI after excitation. Fig. took from [50].

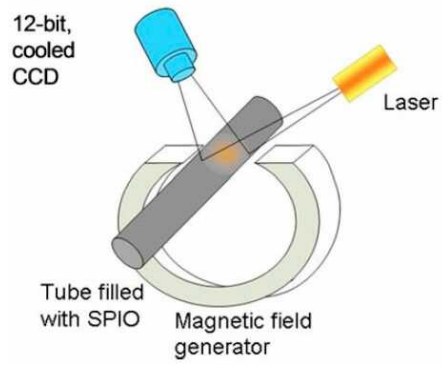


Figure 3.4: Experimental setup used to increase the motion of iron oxide particles in the blood flow torrent. a horseshoe-shaped magnet was used to excite the particles in the simulated capillary to increase the contrast of the CI.

light scattering, which is translated into CI with improved spatial resolution [21, 51].

3.2 Computational models

Regarding the laser, camera, exposure time, among other physical changes in the experimental setup or treatment of the tissue to reduce the scattering coefficient used to acquire the RSI, the feature extraction stage when the raw image is processed is an important task. Although the most used metric to visualize blood vessels in LSCI is the contrast, other processes to the RSI can extract statistical or movement information from the image. The Motion History Image (MHI) uses a set of images to extract a historical representation to trace the movement in a collection of images. The difference between two subsequent images $MH_t = I_t - I_{t-1}$ obtains an estimation of movement in the sequence [52, 53, 54, 1]. Then MH_t is transformed into a binary image T_t using a threshold where 1 represents movement and 0 its absence. Finally, MHI_t represents the motion history image whose value is the cumulative sum of movement found in the sequence (T_t) weighted by the number of frames that have passed since the calculation of T_t . The motion history image can be used to visualize slow dynamics in RSIs such as the growing of maize seed (Fig. 3.5). Given the high noise level and high dynamics in images of tissue with blood vessels, MHI is unsuitable to analyze the dynamics of that type of image.

$$MHI_t = 255 \sum_{k=0}^{f-1} T_t - k \cdot h_k \quad (3.1)$$

$$h_k = \frac{N - k}{M} \quad (3.2)$$

where $M = N(N + 1)/2$ is the summation of N natural numbers so that the summation of all h_k is 1 and h_k is:

On the other hand, the generalized difference method or Fujii method creates a factorial summation of the difference between frames (Eq. 3.3). The technique

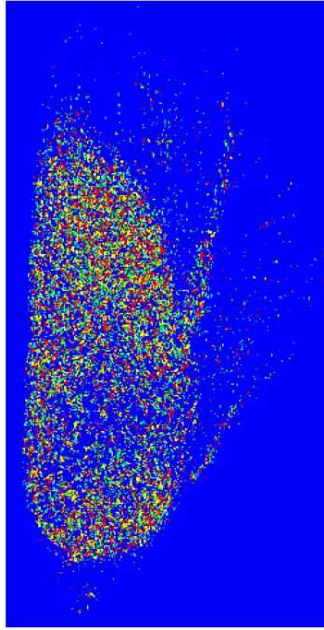


Figure 3.5: Motion history image of growing maize seed.

focuses on representing the motion in the image by detecting the fluctuations between frames. One of the main concerns with this method is the high computational cost due to the factorial subtracting and the low temporal resolution due to the requirements of several frames (up to 60) to compute the representation [55, 56].

$$GD = \sum_k \sum_t I_k - I_k - t \quad (3.3)$$

As explained before, in the RSI the tissue forms homogeneous (dynamic region) and heterogeneous patterns (static region). These patterns can be processed by a contrast representation of the image and other metrics such as local binary patterns or features obtained from a Co-Occurrence Matrix (COM). Some of the features that can be obtained from the COM are the contrast and a homogeneity measure. The COM binary histogram representing the number of transitions between two pixels intensities in the image l to m .

$$COM(i, j) = \sum_{m=1}^M \sum_{l=1}^N \begin{cases} 1, & \text{if } [(I(i, j) = i) \& (I(i + \Delta_i, j + \Delta_j) = j)] \\ 0, & \text{otherwise} \end{cases} \quad (3.4)$$

The COM is calculated using a shifting squared window over the image to be used as a predictor of blood vessels (Fig. 3.6a), selecting the processed neighbors pixels using Δ_i and Δ_j (Fig. 3.6b). The neighboring pixels establish the occurrence of similar pixel values at different directions (0° , 45° , 90° or 135°) as seen in Table 3.1.

angle	Δ_i	Δ_j
0°	2	0
45°	2	2
90°	0	2
135°	-2	-2

Table 3.1: Values of Δ_i and Δ_j to establish the neighborhoods at different angles.

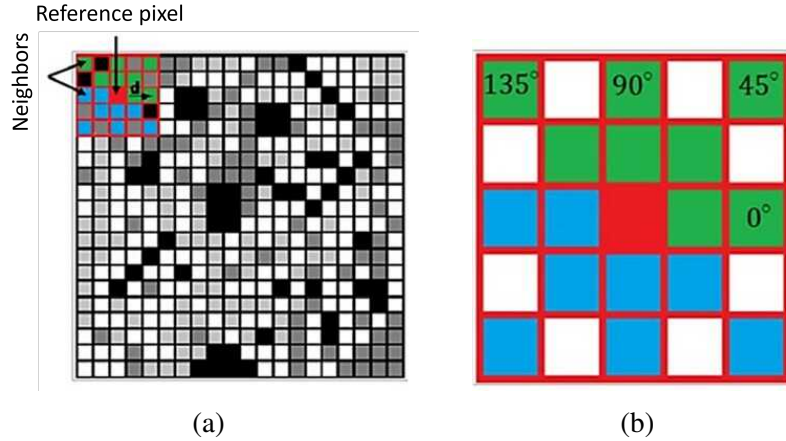


Figure 3.6: Process to compute a homogeneity representation from a RSI. a) RSI and a sliding window of 5×5 , b) directions in the sliding window [57].

3.2.1 Traditional methods for contrast calculation

Some approaches in the optics and computational areas aim to improve the visualization of blood vessels in LSCI. These works can be divided into two main approaches.

Traditional approaches establish a different type of correlation between the pixels in the RSI to compute the CI. These methods use spatial, temporal, or spatio-temporal analysis windows using a squared analysis window with the same size for all the pixels in the RSI. On the other hand, adaptive approaches perform a selection of pixels involved in the contrast calculation by analyzing the neighborhood of each pixel in the RSI. This section briefly discusses the main characteristics of each approach and its main methods.

Traditional approaches in LSCI aim to compute the CI with a fixed neighborhood for all the pixels in the RSI. The main difference between methods in traditional approaches is the dimension from which the pixels are selected to calculate μ and σ (See Eq. (2.1)). Spatial Contrast (sK) considers the pixels in a squared neighborhood sW_p^d centered at p with a size of $d \times d$ (Fig. 3.7a) [6, 58]. Usually, d takes values of 5 when the spatial resolution is more important than a noisy image or 7 when the application requires an improved noise attenuation. Both sizes of d provide a satisfactory compromise between spatial resolution and reliable statistics [16]. The sK provides the best temporal resolution because the method uses one frame at a time to compute the CI [8].

$$sK_{x,y} = \frac{\sqrt{\sum_{i=x-r}^{x+r} \sum_{j=y-r}^{y+r} \frac{1}{d^2} [I(i,j) - \mu_{x,y}^s]^2}}{\mu_{x,y}^s} \quad (3.5)$$

where:

$$\mu_{x,y}^s = \sum_{i=x-r}^{x+r} \sum_{j=y-r}^{y+r} \frac{1}{d^2} I(i,j)$$

$$r = \frac{d-1}{2}$$

An improvement of the sK method occurs when n sK CIs are calculated and

then averaged to obtain only one CI [59, 60, 61]. The resulting image after the averaging is called Averaged Spatial Contrast (asK). The CIs obtained through the asK method lose the characteristic temporal resolution of sK, but it gains greater noise attenuation [62]. The best compromise between temporal and spatial resolution is obtained by averaging 15 frames with a sW^3 , and 5 frames with a sW^5 [60, 59].

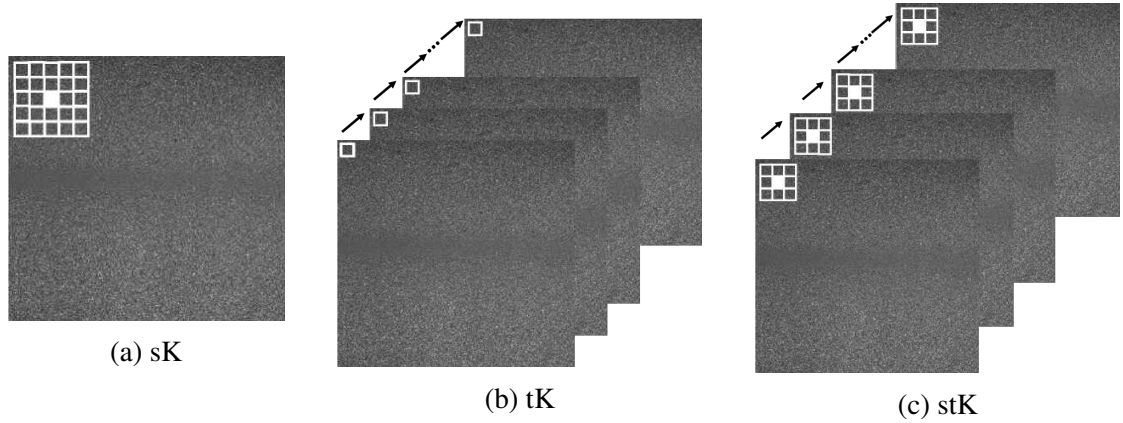


Figure 3.7: Traditional LSCI approaches: (a) sK commonly computed with a bigger analysis window that stK, (b) tK processed with a window of $1 \times 1 \times n$, and (c) stK with a $stW^{3,n}$.

Temporal Contrast (tK) is an approach that analyzes a set of n RSI frames by taking one pixel at a time through all the frames in the set (Fig. 3.7b) [63, 64]; then, contrast is computed as indicates in Eq. 3.6 with a minimum of $n = 15$ to obtain a valid RSI [65]. Since pixels are not processed spatially, tK brings high spatial resolution, a relevant characteristic when smaller blood vessels must be located. The maximum number of frames should be guided by the minimum temporal resolution needed for each particular application. The noise level in the resulting images from tK is higher in comparison with sK and asK [66, 67].

$$tK_{x,y,n} = \frac{\sqrt{\sum_{f=1}^n \frac{1}{n} [RI(x, y, ri) - \mu_{x,y}^t]^2}}{\mu_{x,y}^t} \quad (3.6)$$

$$\mu_{x,y,n}^t = \sum_{ri=1}^n \frac{1}{n} RI(x, y, ri)$$

A combination in the way that sK and tK select pixels is proposed in the Spatial Temporal Contrast (stK) approach is defined through the time and spatial dimensions of a set of RSIs (Fig. 3.7c). Thus, a three-dimensional W is used to compute the contrast in the stK approach. Although certain noise level attenuation is reached, the result is more similar to asK than to sK [66].

3.3 Adaptive processing

Adaptive processing of digital images, as explained in the Section 2.2.1, consists of filtering or shape comparison of an image I using a convolution matrix S , indicating which pixels will be used in the process, adapting itself to the morphology of the analyzed central pixel. Thus, S may change for each pixel in I . The adaptive mathematical morphology is based on the local structuring elements that can change depending on the analyzed pixel. The main difference between adaptive methods is the selection of the convolution matrix S , in which pixels can be selected in different ways, but here the works were grouped in three: The pixel selection by region growing in which the involved pixels are those that are similar to the analyzed pixel by accomplishing a criteria [31, 68], the selection of the best convolution matrix in which depending of the analyzed region the best convolution matrix is selected among a set of predefined S [37, 23], and the adaption of S in which a geometric predefined convolution matrix adapts its properties depending of the neighborhood, i.e. the size of a square or the angle of an elliptical geometric shape [29].

The Morphological Amoeba (MA) aims to construct the structuring element by selecting a set of connected pixels using the geodesic distance. A threshold is used to decide whether a pixel belongs to the structuring element. [68]. A mean filtered

image is used as a reference image because the main limitation of the MA relies on the noise of the image. On the other hand, the region growing approach aims to construct connected structuring elements with a recursive region growing process that minimize a homogeneity function ρ defined in Eq. 3.7. The pixel selection is performed recursively in an 8 connectivity b with less difference with the seed a until S has exactly N elements [31].

$$\forall a, b \in D, \rho(a, b) = |I(a) - I(b)|. \quad (3.7)$$

On the other hand, some methods do not use a threshold in I or a filtered version of I . The selected pixels are those that are connected and satisfy the aggregation condition defined in Eq. 3.8.

$$|RI(y) - RI_x(x)| \leq tr \quad (3.8)$$

Where R_x is the reference image calculated from I , a feature map of luminance, contrast, curvature, thickness [32], gradient [31, 69] or salience filter [70, 28]. Finally, the other type of adaptive methods for image processing, are those that select a structuring element from a set; they do not perform a pixel-by-pixel inclusion analysis. Pixel selection is performed by analyzing the neighborhood to calculate either statistical values to select a structuring element from a set [37, 25, 71, 23] or by calculating the parameters of the structuring element [29]. The Elliptical Adaptive Structuring Element (EASE) selects an elliptical structuring element in a Gaussian filtered image. The EASE aims to estimate three parameters of an ellipse E translated to a pixel p : the minor axis a , the major axis b and the angle of the ellipse ϕ (Fig. 3.8).

$$E_p = E_p(a(p), b(p), \phi(p)) \quad (3.9)$$

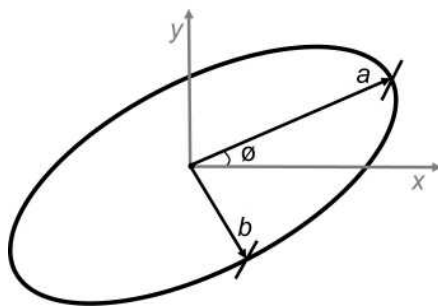


Figure 3.8: Parameters of a elliptical structuring element, the minor axis a , the major axis b and the angle of the ellipse ϕ [29].

Several approaches have been proposed to improve the statistics obtained from a RSI because the contrast is the most used feature to visualize blood vessels in LSCI. Besides traditional approaches, most recent methods aim to compute the contrast representation by using an anisotropic selection of pixels [37, 23, 72] or selecting the window size according to the predominant blood vessel in the RSI [73, 25]. Results suggest that is possible to obtain a CI with an improved noise reduction but reducing the spatial resolution and introducing artifacts in the image [74, 14].

Most recent works suggest that the application of a criterion in W to select the pixels involved in the contrast calculation is helpful to improve the contrast between regions in LSCI [23, 37, 25]. Several analyses have been performed to find the shape of W or the d value that best matches the predominant blood vessel in the RSI to process the contrast with window size and shape adapted explicitly to the present ROIs [25, 37].

The Multi Scale Contrast (msK) approach improved attenuation but lost spatial resolution when processing the CI with the d size of the predominant blood estimated with a granulometry analysis. Although the msK reduced the noise in the inner region of the blood vessel, the squared analysis window decreases the reliability of the statistics in the periphery.

The Three Sizes Contrast (TSK) attempted to improve spatial and temporal

resolution by calculating the contrast with squared window sizes $W = \{3, 5, 7\}$ and depending on the local variance σ_K and σ_I the best W selected. The rationale aims to compute the contrast with the smaller W in the blood vessel region to avoid reducing the spatial contrast and use a larger analysis window W in the static area.

On the other hand, the Anisotropic Contrast (aK) aims to compute the contrast along with the blood flow (Fig. 3.9) [37]. A W of $1 \times d$ is selected by considering an estimated blood flow direction based on the minimization of the contrast gradient between the central pixel p_0 within a set of windows along with different directions a (Eq. 3.10). The main characteristic of aK is considering only the pixels along the less noisy direction. This selection allows aK to address noise attenuation in CIs while it keeps a high temporal resolution using only three frames for contrast calculation.

$$\arg[a_0] = \underset{a \in 0^\circ \rightarrow 180^\circ}{\operatorname{argmin}} \left[\sum_{P \in l} (K_p - K_{P_0})^2 \right] \quad (3.10)$$

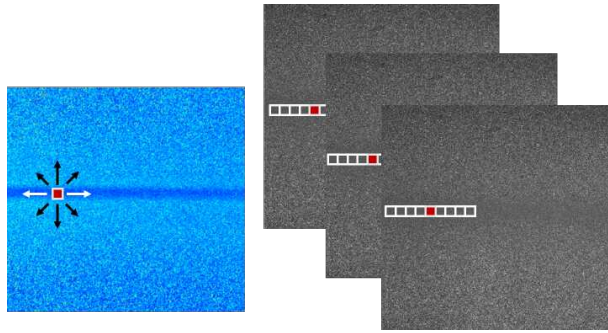


Figure 3.9: Analysis of l directional windows (dark arrows) in the aK approach (left) and, the selected one (in white) for contrast calculation (right). The red dot is the central pixel.

The Space Directional Contrast (sdK) approach performs adaptive computing by a directional analysis in the RSI instead of the temporal contrast as the anisotropic contrast does [23, 71]. The spatial directional contrast performs an analysis frame by frame of the RSI allowing a better pixel selection to obtain improved CI. Furthermore, the frame-by-frame selection avoids generalizing the direction of the blood

flow for contrast calculation in all the frames and considering the dynamic changes among frames. Moreover, the criterion applied over a set V of directional windows v_i with angles of $\{0^\circ, 45^\circ, 90^\circ, 135^\circ\}$ (Eq. 3.11) increases the distance in value between dynamic and static regions which improves the blood vessels visualization.

$$a = \underset{v_i \in V}{\operatorname{argmax}}(\operatorname{var}(v_i)) \quad (3.11)$$

3.4 Discussion

The analysis of blood flow in tissue is relevant due to its biomedical applications. For this reason, current works aim to attack the limitation of the depth in the visualization of blood vessels. Since as the depth of the blood vessel increase, its visualization decreases. In general terms, in LSCI the visualization of blood vessels is affected by the scattering of the surrounding tissue in the ROI [75]. Several techniques that reduce the noise and blood vessel segmentation in CIs have been proposed, but there is still room for improvement. In this section, related works are discussed finding that most of them are focused on the progress of visualization and segmentation of blood vessels.

The main limitation concerning the visualization of blood vessels in LSCI is observed when deep blood vessels are present. Most physical methods to improve the quality of CIs aims to improve the contrast between the static and dynamic regions by making more homogeneous the blurring area of a RSI. The physical methods usually improve the dynamics of the dynamic region by introducing external agents in the blood flow torrent.

Although the methods based on physical changes may increase the contrast between regions in the CIs, they are either expensive or inadequate to their use in sensitive areas like the retina or brain. Thus, to reduce the financial expenses of

Method	Improvement	Invasive	Can be extended
Photothermal [50]	Contrast	yes	yes
Magnetomotive [20]	Contrast	yes	yes
Exposure time [46, 22, 47, 48]	Contrast	no	yes
Laser selection [44, 45]	Depth	no	yes
PCTOC [76, 77]	Contrast	yes	yes
Fluoroscopy [78]	Contrast	yes	yes

Table 3.2: Improvement of CIs in the optics area, most improvements are invasive but the quality of the image can be extended in subsequent stages of the LSCI technique, i.e. in the CI calculation.

change the experimental setup and to avoid invasive methods, several techniques have been proposed. The problem is tackled using computational methods to either extract a different type of information from the RSI through complex feature extraction methods [55, 52, 56, 75]. The main problem of using other techniques besides contrast is the reduced temporal resolution, needing more than 100 frames per analysis. Thus, the contrast representation can be used as a tool to monitor cerebral blood flow [22], retina visualization [15], or visualization of micro-vasculature [14].

Method	Dynamics	temporal resolution	spatial resolution
MHI [52, 53, 54, 1]	slow	no	yes
Fujii [55, 56]	slow	no	yes
COM [79, 75]	fast	yes	no
Optical flow [80]	fast	yes	no

Table 3.3: Features that can be extracted from a RSI.

Because contrast is the most used feature to visualize blood vessels in LSCI, several approaches have been proposed to improve the statistics obtained from the RSI. Besides traditional approaches, most recent methods aim to compute the contrast representation by using an anisotropic selection of pixels [37, 23] or selecting the window size according to the predominant blood vessel in the RSI [73, 25, 71]. Although the improvement in the CI is noticeable, the anisotropic methods introduce artifacts in the image, which means that the original pixels in the image are modified, and groups change their pixel values with a distribution similar to the

structuring element that is being used [37, 74, 39].

Method	overlap W	W	best resolution	noise	artifacts
sK [6, 58]	yes	square	temporal	high	no
tK [63, 64]	yes	point	spatial	high	no
stK [6, 58]	yes	square	spatial	improved	no
asK [59, 60, 61]	yes	square	spatial	improved	no
msK [25, 71]	yes	square	both	improved	no
sdK [23]	sometimes	line	both	improved	yes
aK [37]	sometimes	line	both	improved	yes

Table 3.4: Contrast methods in the literature.

Concerning the adaptive methods to process the contrast images, at this point, it appears that their main limitation relies on the inherent noise present in the images. Current adaptive methods do not perform a reliable pixel selection in noisy images, and being the RSIs only composed of noise, its use is ineffective. The region growing methods such as the amoeba do not work well when the initial seed is an outlier value. On the other hand, the use of salience and gradient methods has problems because in the RSIs there are no borders well defined to allow the method to select a correct structural element. Also, in the region, growing methods that use a threshold to determine whether a pixel is used or not in the calculation have problems because the selection of a suitable threshold is a requirement that limits its use in not noisy images.

Chapter 4

Proposed solutions

This chapter describes the algorithms to compute a feature representation of an image adaptively by selecting the pixels involved in the operations. First, the selects the pixels by using region growing and a threshold to determine whether a pixel is included or not in calculus. Then, the Adaptive Window Contrast (awK) and the Spatially Adaptive Windowing Contrast (sawK) are described. These methods aim to avoid using any threshold in the pixel selection by using unsupervised learning to group the pixels by minimizing the intraclass variance between the static and dynamic regions in the image. Also, a post-processing step aiming to reduce the blobs in the segmented image based on mathematical morphology is presented.

4.1 Adaptive processing by selecting the best size of the analysis window

The method aims to determine the size of the blood vessels present in a LSCI image to establish the size of a squared analysis window used in the contrast calculation. Three steps guide the method: the first step uses a pre-segmentation of the blood

vessels in the image to choose the seeds to perform a region growing process. Then, a diameter map is constructed to use it as a reference to select the appropriate d for each pixel in the image. The proposed method search for a pre-segmentation between the static and dynamic regions in the image by a thresholding process that aims to approximate the segmentation of the blood vessels. However, the binarization process may over-segment the blood vessels. Thus, a skeletonization method obtains the mean shape of the ROIs in the image. Then, the mean shape is sampled, and the selected pixels are used as seeds to perform the process that estimates the blood vessel properties in the image. Later a diameter map with the properties of the blood vessels is reconstructed with the information of the region growing process. Finally, using the diameter map, an appropriate d of W^d is selected for each pixel in the Laser Speckle Imaging (LSI) to compute a CI.

Firstly, the Otsu method estimates an approximated threshold in the normalized CI between $[0, 1]$ in aRSI, searching for the maximum separability between the two distributions in the image: the static and dynamic region. The obtained threshold has a value of $tr \approx 0.5$ for all the images. Then, a binarization process is applied using the threshold to determine if a pixel is a blood vessel or not. The blood vessels were marked as 1 and the static region as 0 by using Eq. 4.1. The binarized image can be over-segmented. The initial seeds may select unwanted pixels in the static region, thus to alleviate this problem and avoid isolated small regions, a morphological erosion with a structuring element of type disk with size 2 was applied. The resulting image is shown in Fig. 4.1b.

$$Ib_p = \begin{cases} 0 & I_p > tr \\ 1 & \text{otherwise} \end{cases} \quad (4.1)$$

A skeletonization morphological operation is used to select appropriate seeds inside blood vessels. With this, an approximate center of each vessel is obtained

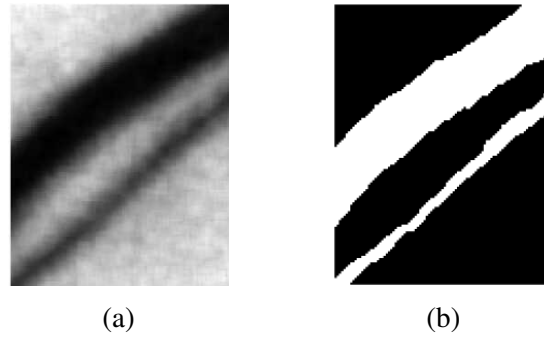


Figure 4.1: Binarization of a RSI. a) RSI, the darker area is the blood vessel, and b) binarization of the RSI after an erosion.

(Fig. 4.2c). Later, spur pixels in the skeleton are removed to avoid the selection of seeds that lay in the periphery of the vessel. Then a subset of pixels is randomly selected to be used in the region growing process. It is important to grow different regions rather than only one to obtain a diameter estimation because of the changes that can occur during the extension of the blood vessels. Using several measurements improves the spatial resolution of measures, leading to a better representation along blood vessels, especially if a bifurcation or different diameters are present.

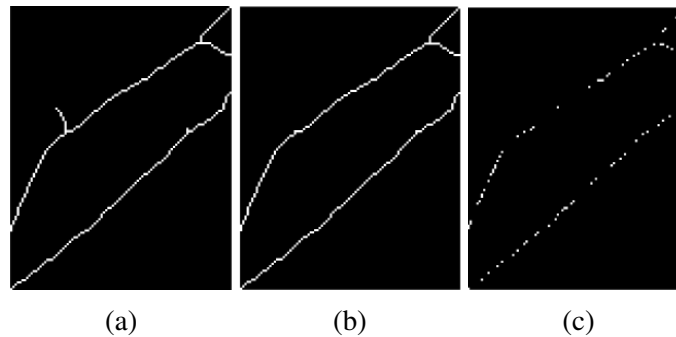


Figure 4.2: Seed selection in an LSCI image. (a) skeletonization, (b) removing of spur pixels and (c) random selected seeds

Then, image I is normalized in the range $[0, 255]$ to apply a region growing algorithm for each seed of the skeleton. Then, the minimum distance between two parallel points in the region r_i was stored cumulatively in a support matrix ma on par with the number of areas that grew in each pixel as a weight map wm . Most times, two adjacent seeds may grow in overlapping regions. The overlapping provided more

information, as if taking several samples of the diameter at each region, each region will contribute to obtaining a better estimation in intersections or bifurcations. The eccentricity was used to perform a validation of the regions that contribute in dm because if the eccentricity equals 0, the region is a circle. It is used because as the region grows through blood vessels, it begins to deform, gaining eccentricity (as seen in Fig. 4.3b). Thus, the diameter map dm_i is the mean of the smallest distance between two parallel points for each r_i accumulated in ma_i and divided by wm_i .

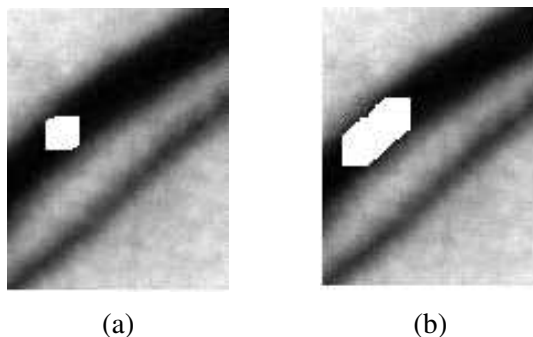


Figure 4.3: Regions that grew in blood vessels with different eccentricities (a) low eccentricity (0.3), ergo, low adjustment (b) eccentricity near 1 (0.9), ergo higher adjustment.

Experiments were performed to know the error between the estimated blood vessel diameter and the actual diameter in distinctive scenarios present in LSCI. The goal is to obtain a similar blood vessel diameter estimation to the ground truth. The diameter is measured in terms of pixels. The used CIs were obtained with the ask method averaging 30 frames to get the less noisy type of CI. For repeatability, three distinctive regions were searched and cropped from the original images: i) when a blood vessel with a distinct diameter is present in a region, ii) when a blood vessel changes its diameter, and iii) when a bifurcation is present in the CI. The region growing process was executed with one seed of each three from the skeletonization to perform the experiments. A threshold of 20 gray values determines whether a pixel is similar to the analyzed pixel. If the difference between the analyzed pixel and the mean of the region is above 20, the pixel is discarded; otherwise, the pixel is included in the region. The search space was limited to $d = 50$ around the analyzed

Algorithm 3 Adaptive processing by selecting the best analysis window

Require: I, dw, δ, etr **Ensure:** Feature map F **Seed selection*

- 1: $CI \leftarrow$ asK of I
- 2: $R \leftarrow$ thresholding of CI using Otsu's method
- 3: $R \leftarrow$ skeltonization of R
- 4: $R \leftarrow R \ominus d : d$ is a disk of size 2
- 5: $R \leftarrow$ random samples of R

**Sizes map retrieving*

- 6: **for each** pixel $p \in R : R_p = 1$ **do**
- 7: $r \leftarrow$ region growing in CI using p as seed
- 8: $ecc \leftarrow$ eccentricity of r
- 9: **for each** pixel $pp \in r : r_pp = 1$ **do**
- 10: **if** $ecc > etr$ **then**
- 11: $wm_{pp} \leftarrow wm_{pp} + 1$
- 12: $wa_{pp} \leftarrow wa_{pp} +$ minimum axis of r
- 13: **else**
- 14: $dm_{pp} \leftarrow 0$
- 15: **end if**
- 16: **end for**
- 17: **end for**

**Feature map construction*

- 18: $F_p = compute(I, \delta, dm)$
-

pixel, enabling the detection of blood vessels with a diameter of at least $(d/2)$. The relative error of the estimated blood vessel was calculated using Eq. 4.2[81], where D_v is a visually estimated blood vessel diameter, and D_c is the blood vessel diameter estimated with the methodology.

$$Err = \left| \frac{D_v - D_c}{D_c} \right| \times 100 \quad (4.2)$$

Fig. 4.4 shows a diameter map obtained with the methodology. The diameter map is a matrix with the same size as the original CI of $m \times n$ where each pixel represents the estimated diameter in pixels. The method can estimate the diameters in straight blood vessels, in bifurcations, and when the diameter changes. It is

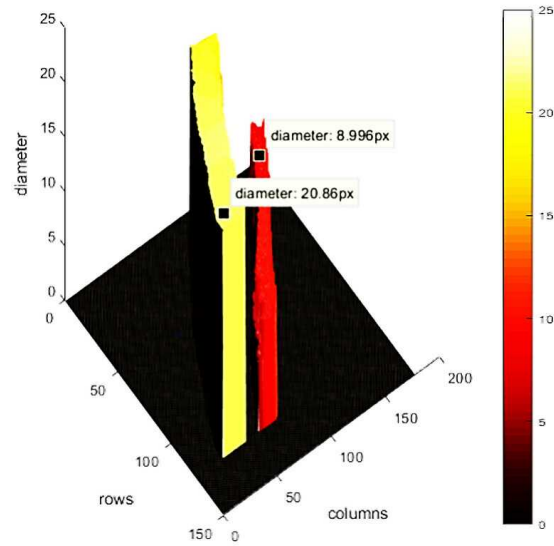


Figure 4.4: example of a diameter map with two blood vessels obtained after applying the methodology.

possible to obtain a diameter map in images with bifurcations where a blood vessel bifurcates into two smaller ones as seen in Fig. 4.5 with an error of $8.13\% \pm 4.55\%$.

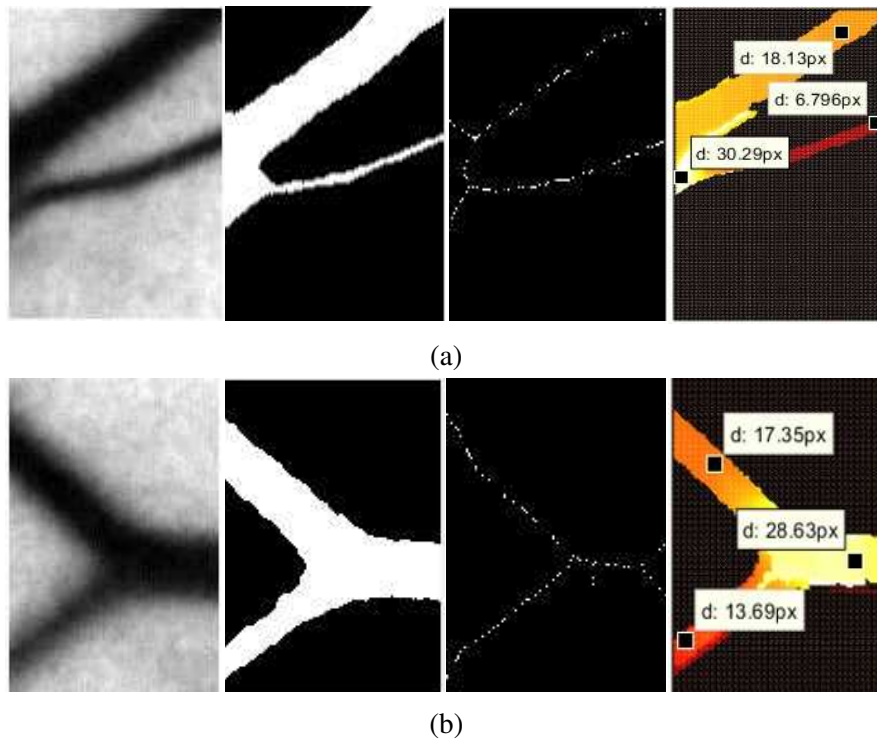


Figure 4.5: Diameter maps obtained in images with bifurcated blood vessels.

4.2 Adaptive processing by pixel selection

Although current methods for LSCIs, obtained an improved temporal resolution by reducing the noise in the CI and the number of frames required to obtain a less noisy image, the spatial resolution and high noise level at high depths ($> 300\mu m$) are still a problem to solve. The main issue regarding the processing of a CIs by a window with a fixed size is that part of the included pixels may not be representative of the ROI (Fig. 4.6a). On the other hand, another problem is the depth of the blood vessels. As the depth increases, the pixels in the RSI combine information from the spatial and dynamic regions. The proposed solution establishes an adaptive image processing technique by selecting the pixels used in the contrast calculation to improve the quality of CIs in LSCI.. The adaptive processing selects the pixels involved in the contrast calculation for each pixel in the RSI (Fig. 4.6b), using a criterion to exclude those that are not representative. Therefore, the analysis may allow larger samples in the contrast calculation to obtain more reliable statistics.

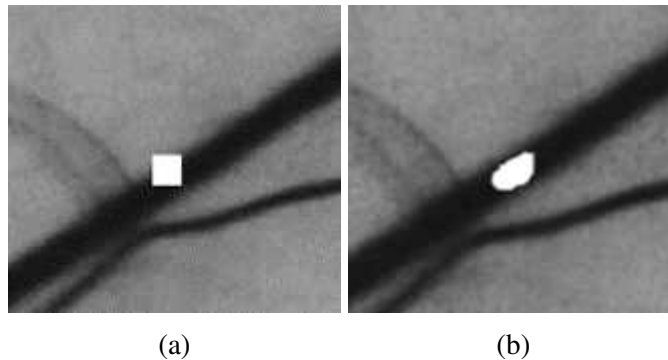


Figure 4.6: Example of an *in-vivo* CI in the torso of a rat where the contrast values are processed by taking pixels over a blood vessel a) with a traditional square window of fixed shape and size, and b) with the proposed adaptive window approach.

This section describes the proposed adaptive approaches for contrast calculation by region growing. Thus, if squared analysis window W_p^d with maximum size d and the central pixel p belonging to a blood vessel is being processed, we aim to obtain a mask S_p^d with values 0 or 1. Where 0 means that the pixel is ignored in the

statistics calculation. The mask can obtain a 1 value if the adjacent pixels pp meet a criterion. Thus, the selection of pixels is based on a similarity measure between the central pixel p of the analyzed region and its neighbor pixels pp around a maximum window size d . The process is shown in Fig. 4.8 introduced in Algorithm 4 and described below in general terms to later explain which differences exist between the proposed methods when the selection criterion is modified.

Traditional approaches use an image R as a reference in which a criterion defines which pixels will be used in the operations (Section 2.2.1). Usually, in the literature, R is a filtered version of the RSI, or the processed image I with a smooth, edge, or salience filter to highlight the necessary features to select the pixels adequately. However, the RSIs contains pixels whose values change considerably from each other because speckles in the image may oscillate between the highest and lowest grayscale value (between 0 and 255 for an 8 bits grayscale image). Thus, commonly used filters could not provide a suitable pilot image. On the other hand, as seen in Fig. 4.7a, the static region has a higher dispersion of values than the dynamic one in a RSI. This distribution is studied using the contrast representation (Fig. 2.1) and is also the reason that it is challenging to define a suitable tr in Eq. 2.3 to determine whether a pixel belongs to a particular distribution. As a result, pixel selection for the mask S may exclude the representative pixels of the region or include noisy pixels in contrast computation. Thus, we studied two solutions to the problems given before; In the proposed method is suggested to use a CI smoothed by a median filter of size s , as the pilot image R since in it the noise is reduced and the contrast between regions increases. The CI is less noisy than the RSI (Fig. 4.7b) but, at high depths, the noise increases then, a smooth filter helps to reduce the more significant outliers (Figs. 4.7c-4.7d). However, noise persists in the image and affects the performance of the criteria for pixel selection.

The adaptive processing of a RSI depicted in algorithm 4 starts by computing the reference image R , which, as explained before, is a median filtered version of the

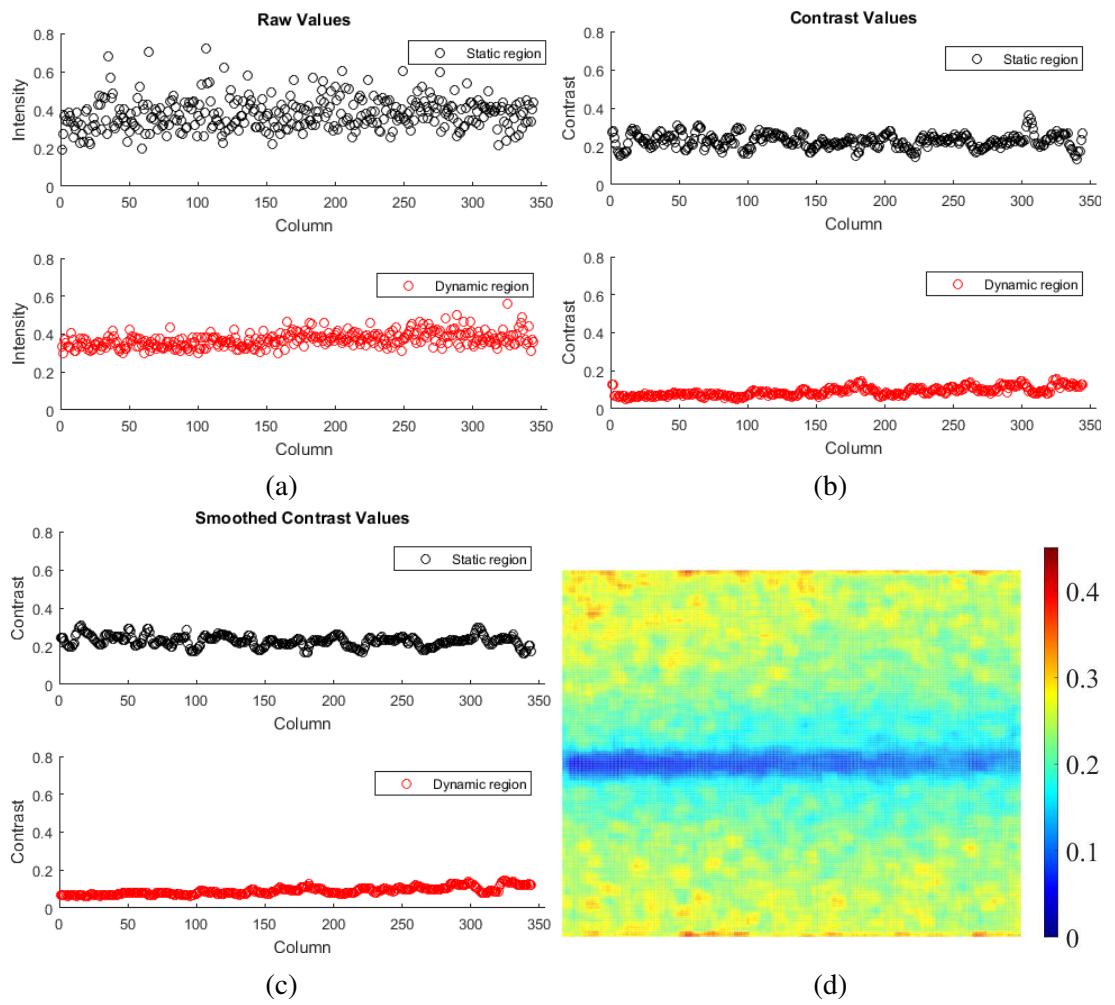


Figure 4.7: Representative scatter plot from the static and dynamic regions in the images: a) RSI of Fig. 2.1, b) CI, and c) smoothed CI; d) the smoothed CI.

asK obtained from the processed image I with a filter size s . Then, for each pixel, p in R a squared binary mask S_p^d with max size d and superimposed in p marks whether a pixel is used or not in an *delta* operation using p as the initial seed, set by default to 1 in S_p^d , and queued into Q (lines 3-5). The criterion used to define whether a pixel is marked as 0 or 1 in the mask can change and is the case of study in this thesis, the proposed criterion are discussed below. The last step of the method consists of operating δ using P , the set of gray levels values in I , being P a subset of I storing the grayscale values of all the pixels marked as 1 in the superimposed mask S_p^d (lines 15-16). A feature map is obtained when applying this process to all pixels p describing the operation δ , and thus, in the specific case when $\delta = K = \sigma^P / \mu^P$ a contrast representation from RSI is obtained. Moreover, S_p^d can be used to process a set of n subsequent frames, as in asK, assuming that there are no significant changes in the spatial location of the blood vessel over the image.

Algorithm 4 General algorithm for adaptive contrast

Require: I, d, s, δ

Ensure: Feature map F

```

1: Compute the pilot image  $R$  using  $\{I, K, s\}$ 
2: for each pixel  $p \in R$  do
3:   Set  $S_p^d \leftarrow 0$ 
4:    $S_p^d(p) \leftarrow 1$ 
5:   Queue  $p$  into  $Q$ 
6:   while  $Q \neq \emptyset$  do
7:      $pp \leftarrow Q.pop()$ 
8:     for each not visited  $p_i$  adjacent to  $pp$  where distance  $< (d - 1)/2$  do
9:       if  $critterion(p, p_i)$  then
10:         $Q.push(p_i)$ 
11:         $S_p^d(p_i) \leftarrow 1$ 
12:       end if
13:     end for
14:   end while
15:    $P \leftarrow \{pp \in I : S_p^d(pp) = 1\}$ 
16:    $F(p) \leftarrow compute(\delta, P)$ 
17: end for

```

4.2.1 Adaptive Threshold Contrast

First, the was developed to analyze the behavior of pixel inclusion by using a threshold approach. The main changes with the general adaptive method rely on using a euclidean distance between the mean of the values in S_p^r and the analyzed pixel. As seen in Algorithm 5 in the changes marked as red, a new pixel is added to S_p^d if the mean of the values in the mask is below a threshold, the analyzed pixel p_i is included in the computing of the operation δ . As mentioned before, one of the main issues in the adaptive processing of images is the selection of a suitable threshold tr to determine whether a pixel is similar or not to the analyzed region.

Algorithm 5 Algorithm for adaptive contrast by thresholding

Require: I, d, s, δ, tr

Ensure: Feature map F

```

1: Compute the pilot image  $R$  using  $\{I, K, s\}$ 
2: for each pixel  $p \in R$  do
3:   Set  $S_p^d \leftarrow 0$ 
4:    $S_p^d(p) \leftarrow 1$ 
5:   Queue  $p$  into  $Q$ 
6:    $m \leftarrow R(p)$ 
7:    $c \leftarrow 1$ 
8:   while  $Q \neq \emptyset$  do
9:      $pp \leftarrow Q.pop()$ 
10:    for each not visited  $p_i$  adjacent to  $pp$  where distance  $< [(d - 1)/2]$  do
11:      if  $\sqrt{(m/c)^2 - R(p_i)^2} < tr$  then
12:         $Q.push(p_i)$ 
13:         $S_p^d(p_i) \leftarrow 1$ 
14:         $m \leftarrow m + R(p_i)$ 
15:         $c \leftarrow c + 1$ 
16:      end if
17:    end for
18:  end while
19:   $P \leftarrow \{pp \in I : S_p^d(pp) = 1\}$ 
20:   $F(p) \leftarrow compute(\delta, P)$ 
21: end for

```

4.2.2 Adaptive Window Contrast

On the other hand, in the awK the smoothed reference image R pixels are grouped into k clusters using the k-means clustering algorithm to overcome the threshold selection problem. The k-means algorithm aims to minimize the intraclass variance between groups without considering the spatial distance. Then, the contrast values in R are substituted by their corresponding cluster label in the range $[1, k]$. In this way, the high variation of values in R is reduced, providing a pixel selection with the same properties to operate δ . Generating a suitable pilot image R (Algorithm 6, line 2). Fig. 4.8 shows the final pilot image, which contains three clusters associated with the static (black), transition (white), and dynamic (red) regions. When the difference among pixels is not abrupt, an analysis window may adapt its shape to the red region.

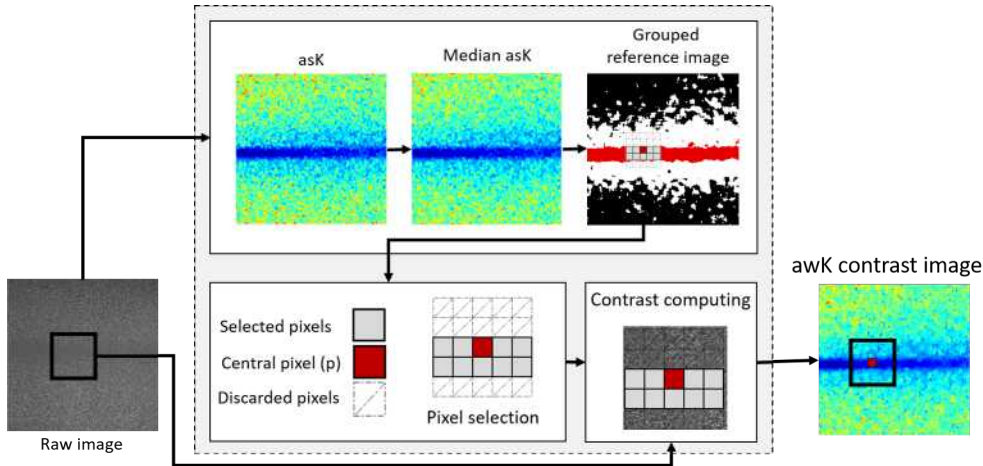


Figure 4.8: Proposed methodology to select the pixels involved in the contrast calculation of each pixel of the RSI.

The pixels involved in the contrast calculation are those adjacent to the analyzed pixel which are evaluated according to the inclusion criterion in Eq. 4.3. If an adjacent pixel p_i meets the criterion is set to 1 in S_p^d and queued into Q (Algorithm 6 lines 7-15). The pixels in S_p^d are evaluated as adjacent at just one time. In this way,

the seed grows at each iteration through the adjacencies of the pixels in S_p^d set to 1.

$$S_p^d(p_i) = \begin{cases} 1, & R(p_o) = R(p_i) \\ 0, & \text{otherwise} \end{cases} \quad (4.3)$$

Algorithm 6 Algorithm for adaptive contrast by unsupervised learning

Require: I, d, s, δ, k

Ensure: Feature map F

```

1: Compute the grouped pilot image  $R$  using  $\{I, s, k\}$ 
2: for each pixel  $p \in R$  do
3:   Set  $S_p^d \leftarrow 0$ 
4:    $S_p^d(p) \leftarrow 1$ 
5:   Queue  $p$  into  $Q$ 
6:    $m \leftarrow R(p)$ 
7:   while  $Q \neq \emptyset$  do
8:      $pp \leftarrow Q.pop()$ 
9:     for each not visited  $p_i$  adjacent to  $pp$  where distance  $< [(d - 1)/2]$  do
10:      if  $R(p) = R(p_i)$  then
11:         $Q.push(p_i)$ 
12:         $S_p^d(p_i) \leftarrow 1$ 
13:      end if
14:    end for
15:  end while
16:   $P \leftarrow \{pp \in I : S_p^d(pp) = 1\}$ 
17:   $F(p) \leftarrow compute(\delta, P)$ 
18: end for

```

4.2.3 Spatially Adaptive Window Contrast

Although the use of adaptive processing obtained significantly higher results than state-of-the-art reported in previous evaluations, in the *in-vivo* images there is room for improvement with more than three observable regions. In the *in-vivo* images, the smallest blood vessels where the blood flow is less than in the predominant ones are combined with the static or the transition regions, which makes the pixel selection less reliable. For this reason, we opted to include a spatial distance and not only the

gray-scale values as a reference to perform the pixel selection. The method is based on the Sequential Linear Iterative Cluster algorithm [?] and modified to select the pixels to avoid a posterized effect. First, a set of k centers are initialized in a regular grid with intervals of $S = \sqrt{\frac{N}{k}}$ in R , where N is the number of pixels in the input image. Then centers are moved at the lowest gradient in its adjacency in a 3×3 neighborhood to avoid outlier values. Next in the assignment step, a label $l(p) = -1$ is assigned for each pixel p . Then in an iterative step, each pixel is associated with its nearest center at a maximum distance of $2S$ based on the minimum distance between the centers and the data points. In the last step, the clusters are updated until clusters no longer change. Then a pixel-by-pixel analysis is performed, and a distance that combines the contrast value and the proximity into a single measure is used to determine whether the pixel is included in the calculation or not (Eq. 4.4). To perform the selection, first, the distance is calculated between the analyzed pixel pp , the central pixel p , and the centers from the grouping algorithm, and if the minimum distance from the three is to p , then pp is set as 1 in S_p^d (Fig. 4.4). Then, the contrast is calculated as the .

$$D = ds + \frac{M}{S}dc \quad (4.4)$$

where:

$$ds = \text{sqrt}(R_{i,j} - R_{x,y})^2$$

$$dc = \text{sqrt}[(i - x)^2 + (j - y)^2]$$

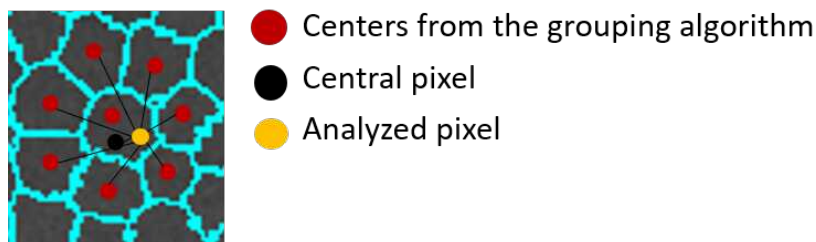


Figure 4.9: Adjacencies of the analyzed pixels with the cluster centers.

4.3 Updating the structuring element

It was noticed that the processing time could be reduced if redundant operations in the region growing process are computed one time following the dynamic programming approach. Thus, the basic algorithm of adaptive processing was modified to reduce redundant calculus without posterizing the image as the duality of the structuring element does, which is the current approach for efficiency in adaptive processing. Instead of recalculating S_p^d for each pixel, the selection is updated using prior information from the previous iteration S_{p-1}^d if the analyzed pixel $p \in S_{x-1}^d$. Then, a translated version of $\in S_{x-1}^d$ without the leftmost pixels is superimposed, S_x^d and its rightmost pixels are added to the analysis queue. In this manner, the pixel selection is the same, and the maximum analyzed pixels in each iteration are reduced to d instead of $[(d \times d) - 1]$.

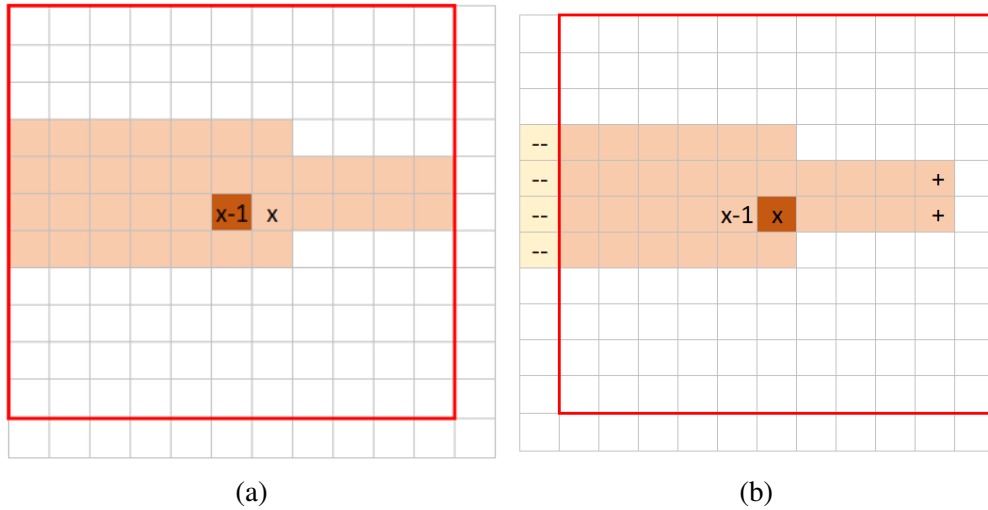


Figure 4.10: Fast adaptive processing, the red line indicates the analysis window with $d = 11$ a) depicts S_{x-1}^r and in b) the pixels marked as "--" are those which were eliminated and those marked as "+" are those added to the analysis queue.

Algorithm 7 Adaptive processing with updating of the structural elements.

```
1: procedure ADAPTIVE CONTRAST( )
2:   for each pixel  $x \in I$  do
3:     if  $x \in S_{x-1}^r$  then
4:       Update  $S_x^r$  using  $S_{x-1}^r$ 
5:     else
6:       Compute  $S_x^r$ 
7:     end if
8:     compute K using  $S_x^r$ 
9:   end for
10: end procedure
```

4.4 Post-processing step: Morphological filtering of binarized data

The proposed methodology aims to be used after a segmentation step, such as thresholding or a segmentation model for CIs. In this case, for validation results, the CIs were binarized with thresholding using a $tr = 0.5$, obtained with the Otsu method. An example of a resulting binary image is shown in Fig. 4.11b where the blood vessel region is the ROI in the image. The image comprises small blobs and artifacts that do not belong to the ROI because they are mainly composed of noise. The small blobs in the segmented image are primarily the result of the oscillating speckles, which are inherent to this kind of image. In order to get rid of the blobs, a morphological erosion with a circle element of the approximate size of the speckle $\lambda = 2$ was applied to eliminate the small elements. Still, it can also cause small holes in the dynamic region to get bigger and a sub-segmentation in the peripheral region. In superficial blood vessels, where the contrast between regions is more extensive, the holes inside the dynamic region are low. However, the holes generated by the low contrast and intense noise are wider at higher depths. To alleviate the problem of the holes, a dilation with a disk structuring element $\lambda = 2$ followed by a region filling operation keeps connected the internal structure of the dynamic region (Fig. 4.11c).

After the processing, it can be observed that small blobs still remain because they have an area larger than the structural element, so they were not eliminated but separated from the dynamic region because of the weakly connection between them. In general terms, the blood vessels in a CI are connected and continuous, represented by the broader structures in the image as observed in Fig. 4.11a. Therefore, the remaining noise can be eliminated by a morphological area opening. In this case, it was determined that structures with area $a \leq 300$ provide an accurate noise removal for our type of images.

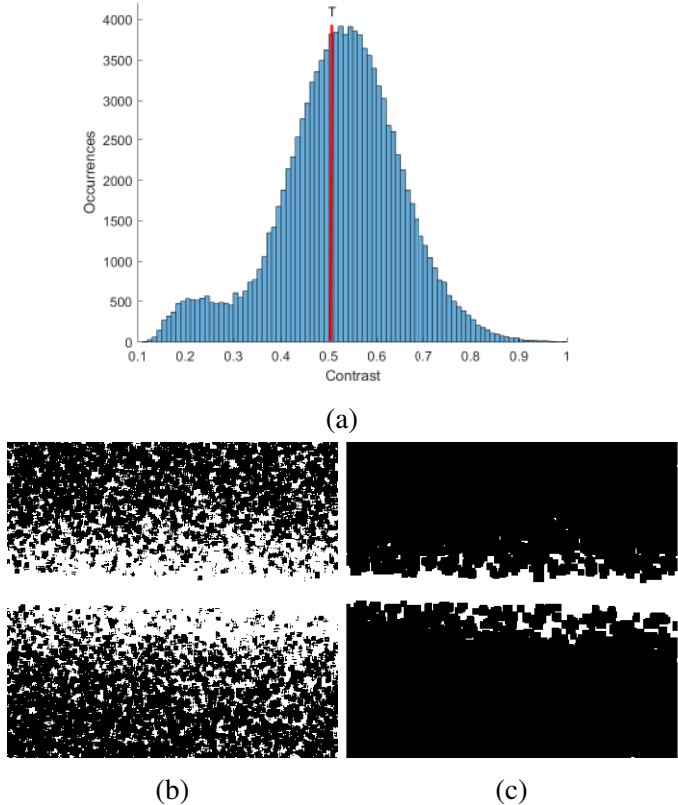


Figure 4.11: (a) Contrast distribution of an LSI image at $0\mu m$, (b) the resulting binary image after automatic thresholding, and (c) noise removal by morphological erosion and region filling.

The RSIs used to test the methodology for filtering segmented CIs consists of the set of *in-vitro* images varying depth from 0 to $900\mu m$, the binarized images were

the asK obtained with $n = 30$ and $d = 5$. The RSIs have dimensions of 344×329 pixels and 280×288 for the straight and bifurcated blood vessels in the image with a speckle size of ≈ 2 pixels. The images were analyzed to know the behavior of the method when the depth of the blood vessel varies. It is important because the RSIs are noisy, and the spatial variations increase with the depth. Then, the results are focused on morphological filtering of small blobs present in the image to improve the location and visualization of blood vessels in segmented CI.

Consider an *in-vitro* RSI at $200 \mu m$ (Fig. 4.12a). The CI allows visualization of straight blood vessels in the dynamic region. Still, in its segmented version, the visualization of the periphery is not trivial because of the noise. Although the segmentation process detected the overall blood vessels, it still carries noise. (Fig. 4.12b). After processing the image with the erosion and the reconstruction, the noise is considerably reduced (Fig. 4.12d). The noise reduction step and the reconstruction separate some structures from the larger blood vessel. Thus, the area criterion is applied to remove the small blobs.

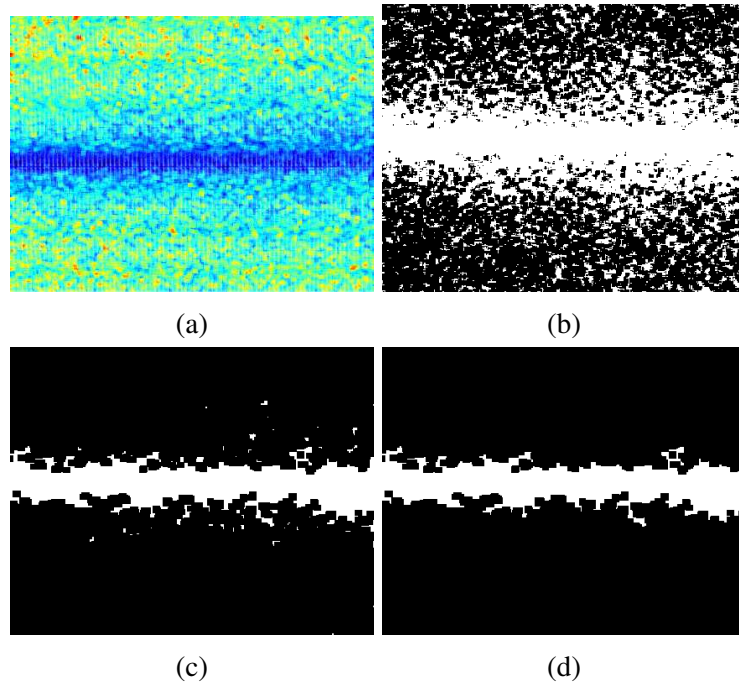


Figure 4.12: In-vitro blood vessel at $200 \mu m$: (a) contrast representation, (b) thresholding, (c) morphological erosion and region filling, (d) elimination by area criterion.

On the other hand, let's consider a $600 \mu m$ where the noise level is higher. Although even the intense noise in the image is higher than at a depth of $200 \mu m$, Fig. 4.13 show that the blood vessel visualization is affected, even with high noise condition, the method can reduce the intense amount of noise preserving the ROI. In conclusion, this method surges from a necessity to eliminate the blobs caused by the fluctuating speckles and the inherent noise of the CI in LSCI. The method allows the reduction of small blobs outside the blood vessels and also reconnects the holes in the ROI caused by the fluctuations in the contrast values of the CIs.

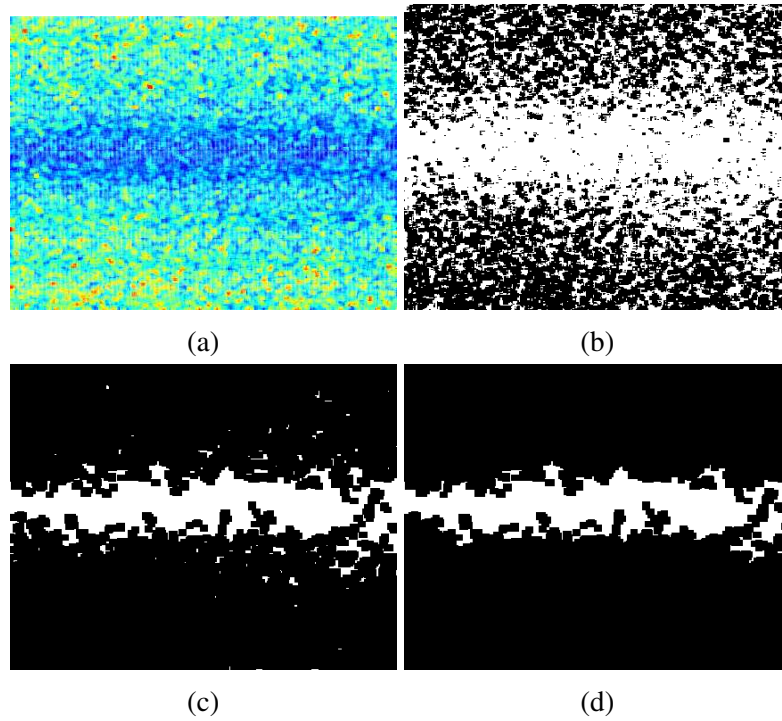


Figure 4.13: In-vitro blood vessel at $600 \mu m$: (a) contrast representation, (b) thresholding, (c) morphological erosion and region filling, (d) elimination by area criterion.

Chapter 5

Experiments and results

This chapter describes the performed experiments during the thesis work and its results. The first section describes the parameter selection for the awK followed by the validation and comparison with the other proposed methods and state-of-the-art. After that, the experiments consist of testing the methods under different conditions. The experimental variables considered were depth, exposure time, blood flow, and the number of frames.

5.1 Data description

This section briefly describes the experimental setups of the data to perform the experiments. The data were acquired from different sources of previous works[82, 66]. A basic experimental setup to obtain the images consists of a laser with an optical diffuser to illuminate homogeneously the sensed object, and a camera to sense the photons that interacted with it.

A experimental setup such as the depicted in Fig. 5.1a was used to simulate *in-vitro* blood vessels in tissue image to control the factors that impact the CIs

such as the blood flow velocity, depth, or exposure time. Skin phantoms were used for the dermis and epidermis with similar optic characteristics to the skin (Fig. 5.1b) [83]. The dermis was simulated with a resin containing titanium dioxide (TiO_2 1.45 mg/mL), while the epidermis was made of a silicone layer (polydimethylsiloxane) containing TiO_2 powder (2 mg/mL). The TiO_2 concentrations are used to mimic the scattering properties of dermis ($\mu_s = 2\text{mm}^{-1}$) and epidermis ($\mu_s = 3\text{mm}^{-1}$), respectively. Glass capillaries (thinXXS Microtechnology AG, Germany) with an inner diameter of $700\mu\text{m}$ and $300\mu\text{m}$ were used to simulate straight and bifurcated morphologies of the blood vessels respectively. To simulate the blood flow an infusion pump (Model NE-500 New Era Pump System Inc.) inject an intralipid with 1% concentration into the microchannel via Tygon tubing. Next, to test the validity of the algorithms in more realistic environments, we used *in-vivo* images of a rat torso. For *in-vivo* experiments, a mouse dorsal window chamber model was used [82]. In short, the window chamber is a surgical preparation in which one full thickness of the skin is suspended between titanium frames. A microvascular network is readily visible from the subdermal side of the chamber; the epidermis of the intact skin thickness is visible on the other side. The experimental setup used to obtain the set of raw speckle images (Fig. 5.1) consists of a coherent light source (He-Ne laser at 632.8nm) that illuminates either the skin phantom or the mouse dorsal window homogeneously through a diffuser (Model ED1-C20, Thorlabs Inc.). A CDD camera (Retiga 2000R, Qimaging), equipped with a zoom lens (NAVITAR ZOOM 700), was employed to capture the RSIs with an exposure time of 10ms and speckle size of $\approx 7.9\mu\text{m}$ [12, 43]. To mitigate specular reflectance from the samples, a polarizing filter was mounted in front of the zoom lens and perpendicularly oriented to the polarization of the incident light.

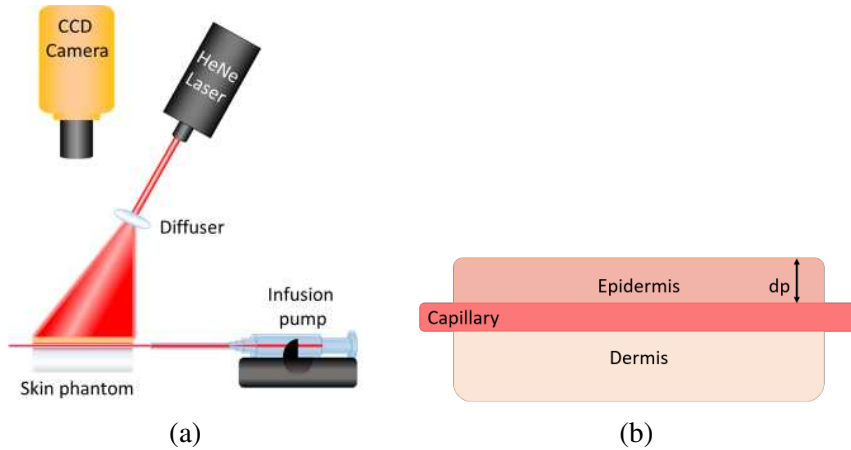


Figure 5.1: a) Experimental setup used for the acquisition of *in-vitro* RSIs and b) skin phantoms used to simulate blood vessels at different depths (dp), three layers were simulated, epidermis, capillary and the dermis.

5.2 Model selection of adaptive window contrast

A parameter analysis was performed to identify the best values and their effects. For the pilot image R , two classical contrast approaches were used: tK to exploit the higher temporal resolution in the images, and asK to compare the improvement reached by pixel selection. $s = \{3, 5, 7, 9, 11\}$ were considered for the median filter applied to R before the clustering process; larger values are not analyzed since they can significantly attenuate the edges between regions. As mentioned before, the transition region is analyzed in this work, then at least three regions are considered but there are not a large number of possible regions of interest. Then, the number of clusters $k = \{2, 3, 4, 5\}$ was analyzed. For the maximum size of S , $d = \{5, 7, 9, 11\}$ values were taken into account.

A statistical model was employed to know the overall effects of the parameters in the CNR. The experiments were performed with adjusted means for each distance $t = \{5, 7, 9, 11\}$ to ensure a valid result in the periphery of the blood vessels. The two datasets, *in-vitro* and *in-vivo*, were considered in the analysis, parameters are resumed in Table 5.1.

Name	Factor	Levels	Values
Pilot image	R	2	asK,tK
Filter size	s	4	0, 3, 5, 7, 9, 11
Number of clusters	k	3	3, 4, 5
Window size	d	4	5, 7, 9, 11
Distance	t	3	3, 4, 5, 7, 9, 11

Table 5.1: Parameter values used to perform the model optimization.

The analysis of variance for the model with one, two and three terms is presented in Fig. 5.3 for the *in-vitro* and *in-vivo* datasets. The F-score and p-value show a significant effect for principal effects in both cases with a $F=305.76$, $p=0.00$ for *in-vitro* and a $F=139.91$, $p=0.00$ for the *in-vivo* samples. Showing that most of the interactions between two terms and all the interactions with three terms can be neglected with a $p=1$ for both datasets (Table 5.3). The Fig. 5.6 shows the standardized effects for the statistical models with $\alpha=0.05$. All the terms have a significant impact on the CNR computed in the periphery of the blood vessels with the proposed awK method. And most of the interactions with two factors are on the borderline of significance (1.96).

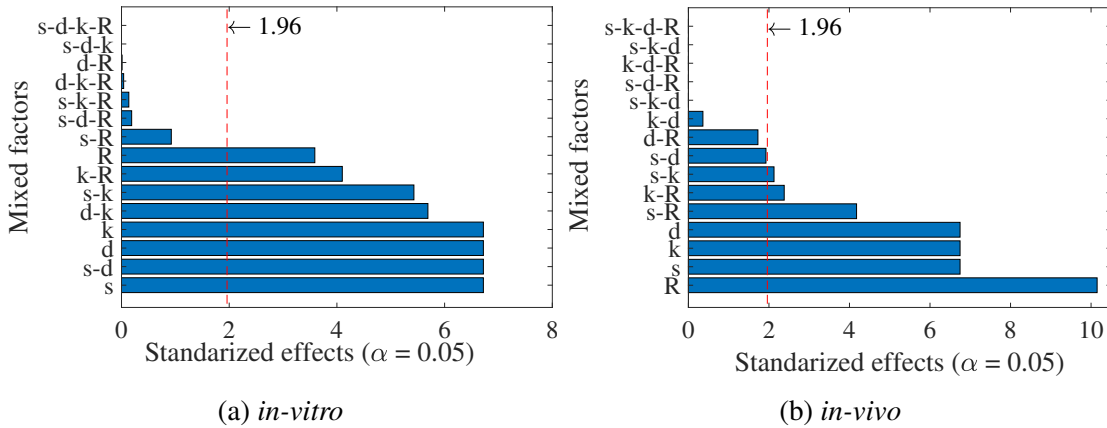


Figure 5.2: Standardized effects for the statistical model. a) images and, b) *in-vivo* images.

Thus, a general linear model with principal effects was fitted to know the effects in the evaluation metric. Therefore, Fig. 5.6 shows the main effects of the parameters

in the model. The effects are similar for both datasets for the pilot image, the filter size, and the maximum size of the structural element, having the most strong effect for the *in-vitro* samples (F=587.23, p = 0.00). The smooth filter also positively correlates with the CNR, which means that the more the filter size increases, the better the CNR is. The correlation may be partly because the grouping phase can designate better clusters. In general terms, the maximum CNR is obtained with a filter size of 11 since the pilot image becomes less noisy, improving pixel selection for contrast calculation. On the other hand, for the window size, in *in-vitro* images with straight blood vessels and *in-vivo* images, the CNR is maximum with the larger convolution matrix. In opposition, a higher number of clusters negatively impact the CNR. Although a higher number of clusters means a more detailed region distinction, it can lead to a posterized effect or a reduction in the possible number of pixels to compute the statistics, in contrast to the maximum size factor. In the *in-vitro* images, the analysis shows that 2 clusters maximize the CNR. This reduction in the CNR is because only two layers were simulated, the blood vessel with only one depth and the static region. For the *in-vivo* images, according to the analysis, three clusters maximize the CNR and also correspond with the number of regions identified as necessary (sufficiently different) in the unsupervised segmentation (F=349.66, p = 0.00). Thus, in consequent experiments with the proposed approach, the model parameters were fixed at those that maximize the CNR in each dataset: $\{R = tK, s = 9, k = 3, d = 11\}$ for the *in-vitro* and $\{R = sK, s = 9, k = 3, d = 11\}$ for the *in-vivo*. Fig. 5.4 shows that $d = 11$ provides the best CNR in *in-vitro* images at $0\mu m$ depth.

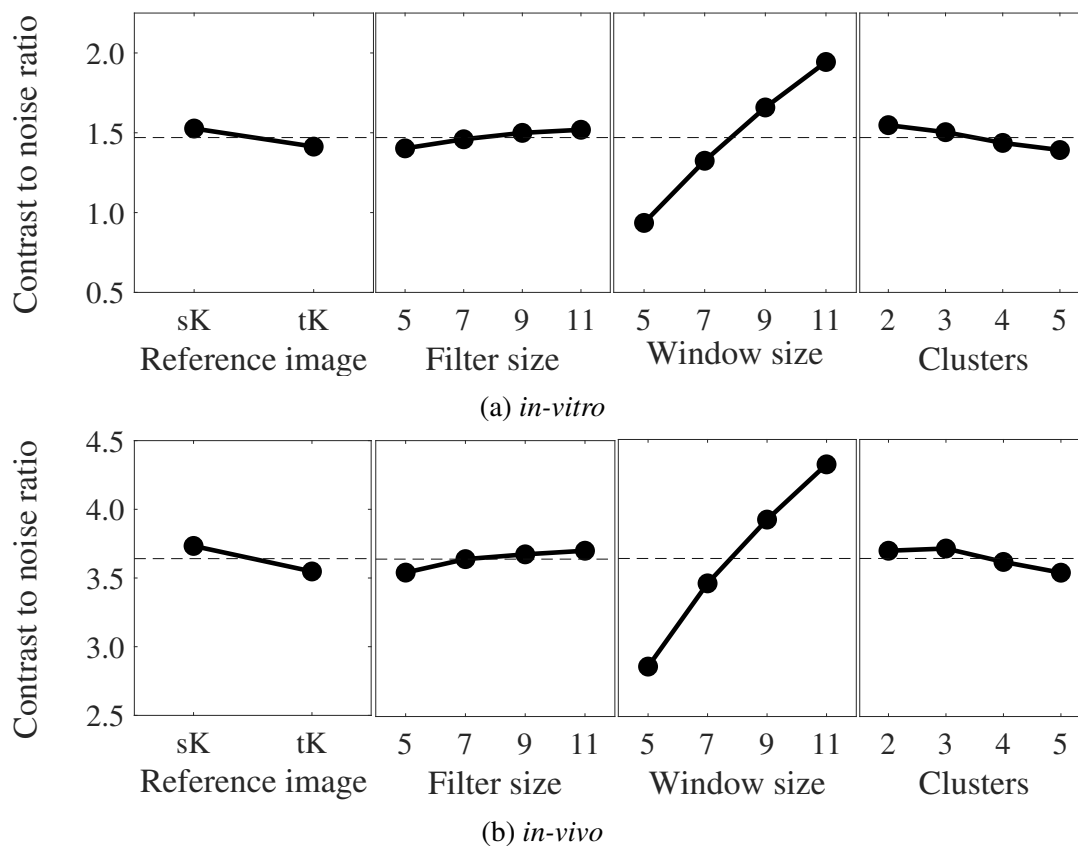


Figure 5.3: Comparisons of the CNR obtained by parameter.

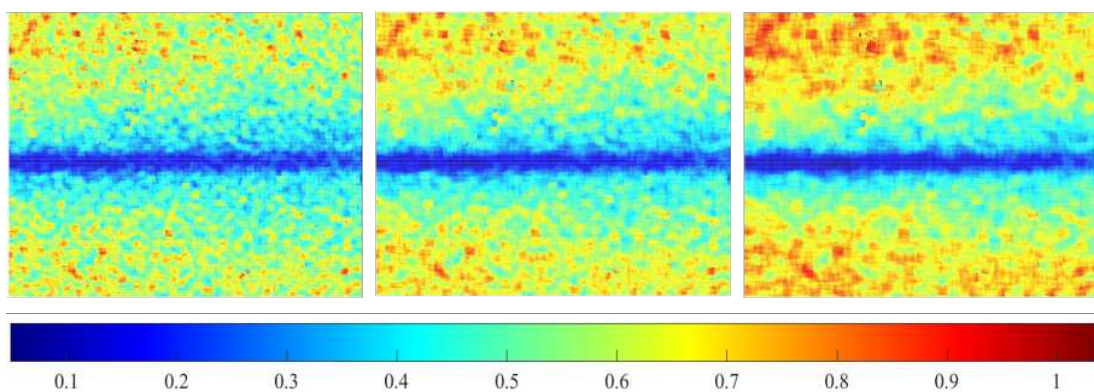


Figure 5.4: Comparison of the CIs obtained by varying the window size d in a *in-vitro* image at $0\mu\text{m}$ depth; results for $d = \{7, 9, 11\}$ are shown from left to right.

Table 5.2: Analysis of variance for the full-factorial models.

Factor	F-score	p-value	Factor	F-score	p-value
One term	305.76	0.00	One term	139.91	0.00
s	247.42	0.00	s	54.76	0.00
d	587.23	0.00	d	27.60	0.00
k	180.23	0.00	k	349.66	0.00
R	12.93	0.00	R	103.03	0.00
Two terms	6.41	0.00	Two terms	2.27	0.00
s - d	10.75	0.00	s - d	2.02	0.03
s - k	5.75	0.00	s - k	1.86	0.05
s - R	1.08	0.35	s - R	7.90	0.00
d - k	6.12	0.00	d - k	0.69	0.71
d - R	0.03	0.99	d - R	3.39	0.01
k - R	7.93	0.00	k - R	2.21	0.08
Three terms	0.30	1.00	Tree terms	0.11	1.00
s - k - d	0.15	1.00	s - k - d	0.08	0.99
s - k - R	0.53	0.85	s - k - R	0.21	0.99
s - d - R	0.48	0.89	s - d - R	0.13	1.00
k - d - R	0.32	0.96	k - d - R	0.07	1.00
Four terms	0.02	1.00	Four terms	0.00	1.00
s - k - d - R	0.02	1.00	s - k - d - R	0.00	1.00

(a) *in-vitro* images.

(b) *in-vivo* images.

5.3 Experiments by depth

The quality of CIs in LSCI is affected by the depth at which the blood vessels are. Thus, an experiment was designed to analyze and validate if the adaptive processing is capable of improving the CI under these restrictions.

A set of 300 images varying the depth ($dp = \{0, 200, 400, 500, 600, 700, 900\}$ μm) of simulated straight and bifurcated blood vessels (Sec. 5.1) is used to analyze if the method improves the image quality at different depths. The *in-vitro* CIs have dimensions of 344×329 for straight blood vessels and 280×280 pixels for the bifurcated ones. To validate the method in more realistic environments, a set of 120 *in-vivo* images was used with dimensions of 1040×1392 pixels with 2 pixels/mote.

The CIs were obtained with the proposed adaptive processing methods and state-of-the-art methods. Then the CNR was measured in the periphery of the blood vessels, varying the distance $t = [3, 4, \dots, 10]$.

Fig. 5.5 show the comparison of asK, sdK, aK, the modified amoeba aawK and the proposed methods awK and sawK. The comparison shows the CNR for each depth paired with the analyzed method to establish a difference between depths. It is observed that the awK and the sawK improved the CNR for all the depths compared with state-of-the-art methods, results which are not obvious because the already published methods for adaptive processing aK and sdK show a reduced CNR for all depths. Showing that a pixel selection approach may overtake those methods that select a predefined analysis window from a set to perform a predetermined pixel selection in a certain angle or direction.

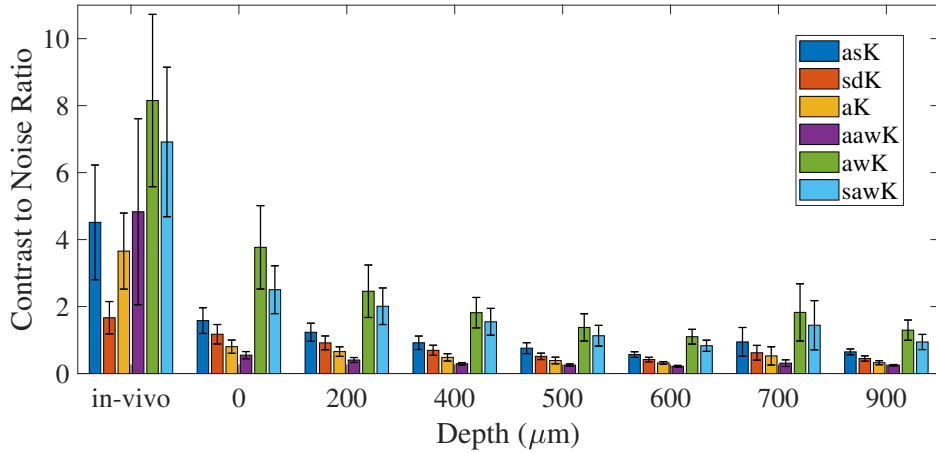


Figure 5.5: Contrast to noise ratio obtained per each depth with the proposed method and the state of the art.

The data were grouped by method for each dataset to measure the statistical significance. The Analysis of Variance (ANOVA) showed a significant improvement in the CNR among datasets between methods with $\alpha = 0.05$. It shows a significant improvement for the *in-vivo* ($F = 50.55$ and $p = 0.00$) and the *in-vitro* images ($F = 69.98$, $p = 0.00$) which mean values are presented in Fig. 5.6a and Fig. 5.6b

respectively. The multiple comparisons using the Tukey method with $\alpha = 0.05$ show that the awK method obtained the highest CNR followed by the sawK as seen in Table 5.3a. On the other hand, in the *in-vivo* comparisons, the statistical method grouped the awK and the sawK as the best competitors in the comparisons obtaining the highest CNR, leading to the state-of-the-art adaptive methods (sdK and aK) as the worst performers in this experiment (Table 5.3a).

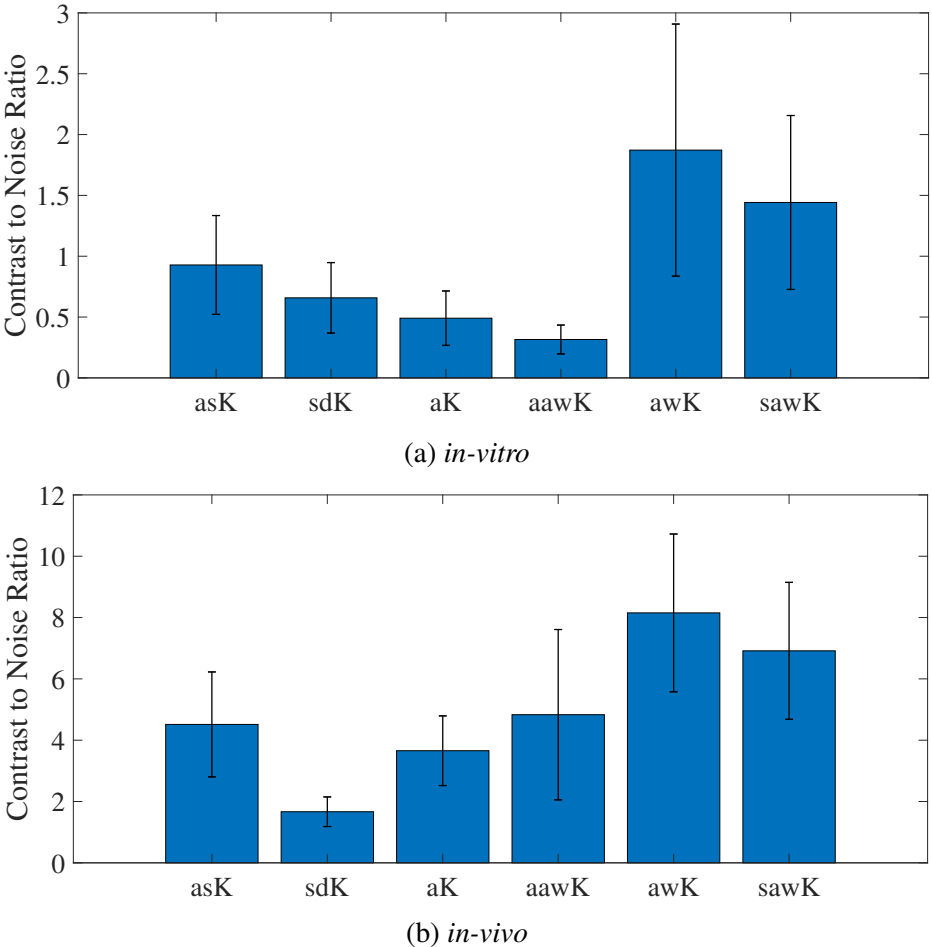


Figure 5.6: Principal effects of the parameters in the CNR. a) *in-vitro* images varying the dept and b) *in-vivo* dataset. The selected parameters of the model are those that maximize the CNR.

Table 5.3: Multiple comparisons of the results with Tukey and $\alpha = 0.5$.

Method	Group
awK	1
sawK	2
asK	3
sdK	4
aK	4
aawK	5

(a) *in-vitro* images.

Method	Group
awK	1
sawK	1
asK	2
aawK	2
aK	3
sdK	4z

(b) *in-vivo* images.

A qualitative comparison between the CIs was performed for images with blood vessels at 0, 200, 400, 500 μm and *in-vivo* CIs. It is observed that the awK and asK increased the contrast between regions in the images (static and dynamic), and the noise was improved in the transition region, seen as a homogenization of the speckles in the *in-vitro* images. Although the contrast improvement was not more significant as in the sdK, the increased noise and the loss of spatial resolution dimmed the increase of quality in the CI. The awK and asK also increased the image quality even in the bifurcated blood vessel at 500 μm . In the *in-vivo* images, the noise is more prominent in the sdK, and aK, as contrasted with the asK. The awK and asK show a great noise reduction without vanishing small blood vessels and areas with less blood flow, such as the horizontal blood vessel from the leftmost upper region, showing a significant improvement in the image quality not only in the quantitative aspect. The most important difference between the proposed methods is in the noisy pixels in the periphery of the blood vessels. Adaptive methods establish a well-defined periphery without introducing noise such as the sdK, asK and aK does. The improvement is because the plasticity of the pixel selection avoids the noise generated by isolated pixels since the shape varies according to the analyzed region without being affected by them. Thus, the proposed approach shows that the noise can be reduced by using an analysis window of larger dimensions ($d > 5$) for contrast calculation without losing the visual definition of the ROIs.

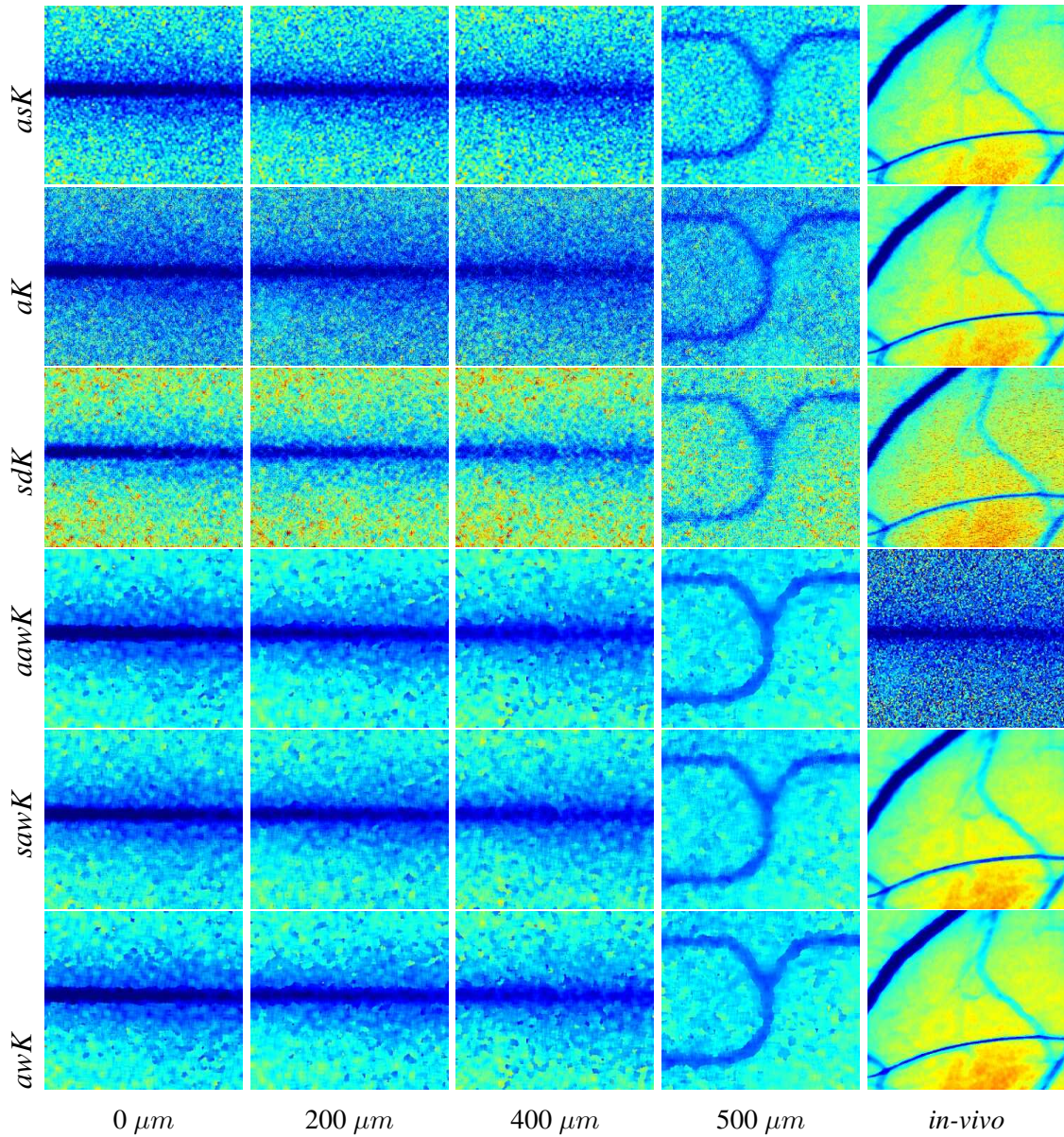


Figure 5.7: Qualitative comparisons of the CIs among methods varying the depth.

A representation with the number of pixels used to compute the CI was obtained to perform a comparison between the dynamic methods. The size representation is defined as $Z_p = |S_p^d|$ (Fig. 5.8). The worst performance was obtained by the aawK method. Combined with the restrictive growing of S , the technique is susceptible to noise and outlier values due to the geodesic distance. For the *in-vivo*

images, the aawK used the desired analysis window of 11×11 (red) mainly in the center of the blood vessels, but in contrast, small sizes were used along almost all the images. For the *in-vitro* images, the aawK does not perform well because the smallest analysis window of 3×3 (blue) was used in almost all the images, and the method had problems with identifying the periphery of the blood vessels because of the noise. In contrast, the awK and the sawK used the analysis window of 11×11 in almost all the images, with the exception of the periphery of the blood vessels and transition regions. As seen in Fig. 5.8, the difference between the awK and the sdK is in the identification of the ROIs. Meanwhile, in the awK, the analysis window size depends on identifying the regions with the correct number of clusters: the blood vessel, the transition region, and the static region. Thus, the limitation of the awK is given by blood vessels with a distinct blood flow velocity. If the blood flow varies, the separation between regions may not be adequate. On the other hand, the sawK separates well the ROIs independently of the blood flow, but its limitation is given by the good selection of the parameters (separation between regions and spatial distance influence).

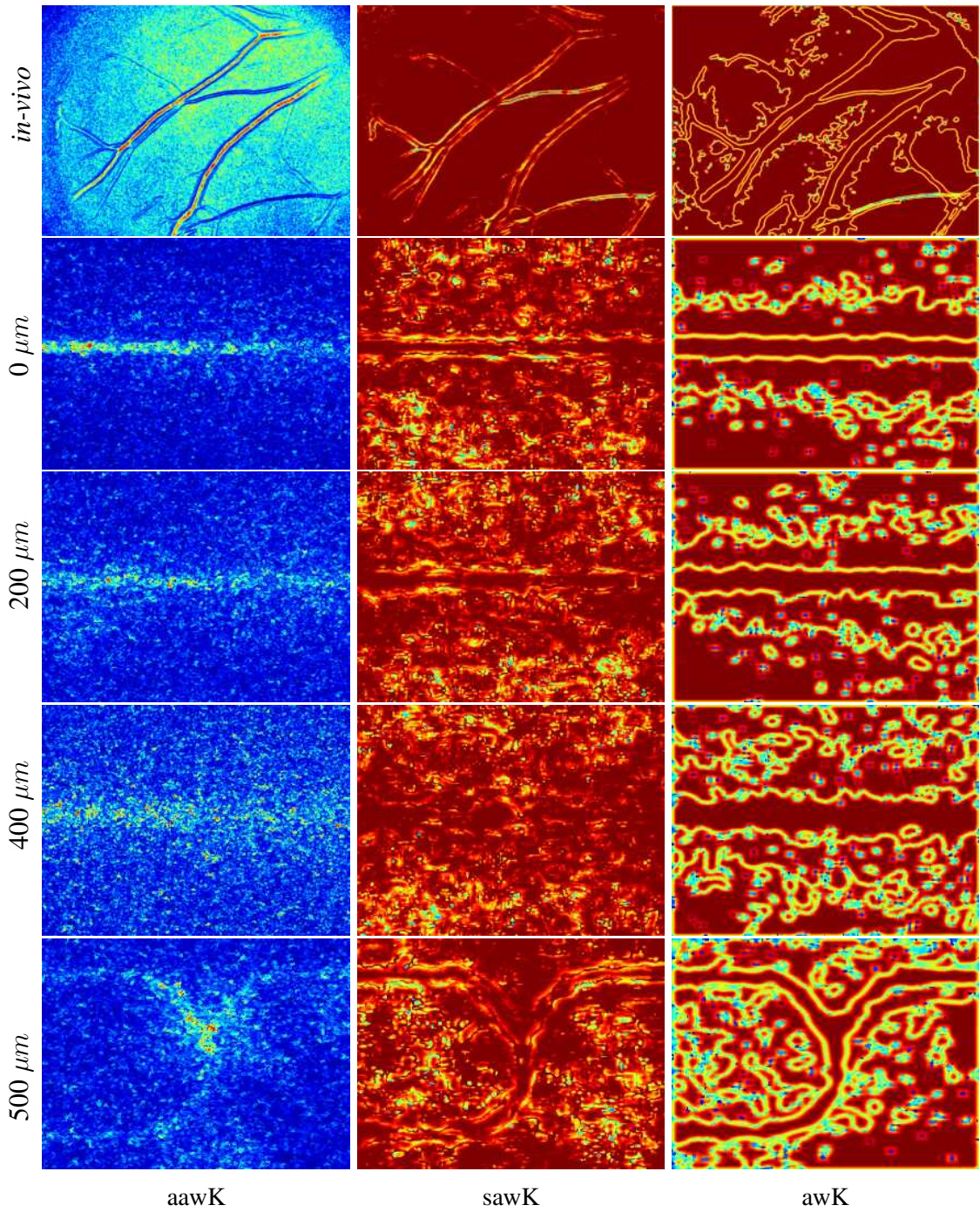


Figure 5.8: Comparison of the size maps for the adaptive processing of contrast images varying the depth and the adaptive method. The blue color represents a size of $d = 3$ and the red color a $d = 11$.

5.4 Temporal resolution

To analyze the temporal resolution to understand the relationship between the number of frames n and the CNR. The analysis was performed for the methods in the state of the art to have a reference for comparison purposes. The proposed experiment compares a set of mean averaged CI obtained for each $n = 1$ to 30, then the CNR was calculated in the periphery of the blood vessel for each image. The used data consists of the *in-vitro* and the *in-vivo* images using 30 frames for each depth and *in-vivo* image. A comparison of the adaptive methods is presented to know the behavior of the techniques by varying n . As seen in Fig. 5.9, the CNR stabilizes from about $n > 15$ but the greatest changes occur from $n = 1$ to 5. The statistical analysis of multiple comparisons depicted in Table 5.4 does not present significant changes until $n = 27$ (multiple comparisons with Tukey with $\alpha = 0.5$). Thus, the best n for adaptive processing is 1 to 5. Where 3 frames have the same quality as 26 frames for high temporal resolution. And the best n for improved spatial resolution is in the range of 27 to 30 frames.

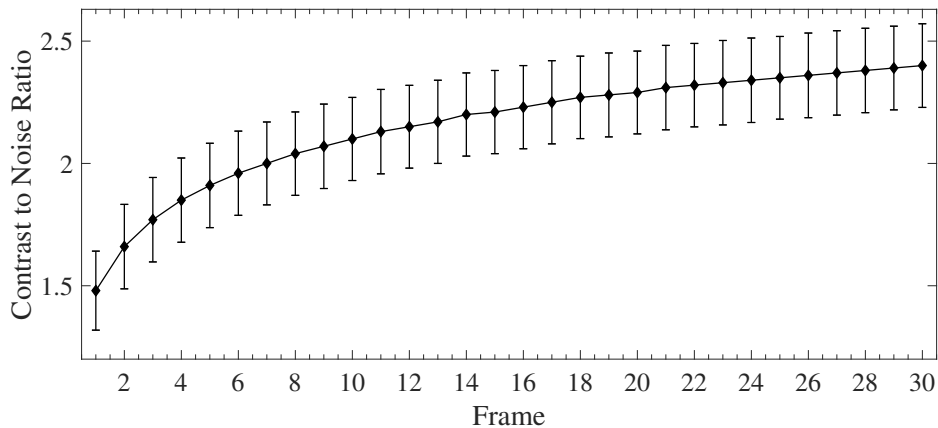


Figure 5.9: Comparison of the contrast to noise ratio obtained varying the frames used to compute the contrast image for the adaptive methods.

Table 5.4: Multiple comparisons for the number of frames used to compute the CIs in the adaptive methods.

Frame	1	2	3	4	5	6	7	8	9	10	11	12	13	14	15	16	17	18	19	20	21	22	23	24	25	26	27	28	29	30
						1	1	1	1	1	1	1	1	1	1	1	1	1	1	1	1	1	1	1	1	1	1	1	1	1
				2	2	2	2	2	2	2	2	2	2	2	2	2	2	2	2	2	2	2	2	2	2	2	2	2	2	2
Group			3	3	3	3	3	3	3	3	3	3	3	3	3	3	3	3	3	3	3	3	3	3	3	3	3	3	3	3
			4	4	4	4	4	4	4	4	4	4	4	4	4	4	4	4	4	4	4	4	4	4	4	4	4	4	4	4
	5	5	5	5	5	5	5	5	5	5	5	5	5	5	5	5	5	5	5	5	5	5	5	5	5	5	5	5	5	5

On the other hand, the proposed awK and sawK obtained the higher CNRs even at $n = 1$. The result suggests that fewer images are required to obtain a CI with higher or the same quality than the traditional methods, even using more frames in the contrast calculation. Thus, the proposed methods increase the contrast in the periphery of the blood vessels even from processing the CIs using the least number of frames ($n = 1$). Also, in general terms, the proposed methods obtained the highest CNRs for all the frames (from 1 to 30) followed by the asK.

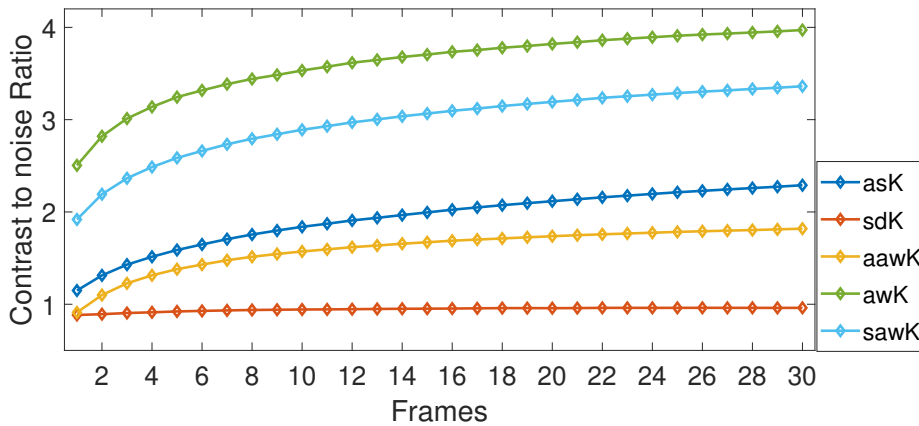


Figure 5.10: Comparison by methods of the contrast noise ratio obtained by varying the number of frames used to compute the contrast image.

5.5 Effect of exposure time

In general, the exposure time is an essential factor of study in acquiring a CI, if the exposure time is lower than the correlation time of the speckles in the images or insufficient, the visualization of blood vessels may be affected. On the other hand, if the exposure time is high, the blurring pattern in the dynamic region of the images may increase, providing better visualization of blood vessels at shallow depths. But also, the periphery of the blood vessels may be dismissed at higher depths because the scattered speckles may increase, increasing the transition region in the CIs, and thus affecting the spatial resolution. The main drawback of increasing the exposure time in a real-time application is the reduction of temporal resolution. More time is required to image a region and thus the impossibility of image tissue in motion. This section presents the experiments and results varying the exposure time and depth. Experiments were performed by varying the CCD camera exposure time and depth of the blood vessels in the image. Also, the inherent comparison of the investigation is discussed for validation purposes.

The analyzed exposure times and depths were $et = \{86, 150, 248, 521, 1058, 1897, 3758, 5796, 8855, 11327, 15996, 20538, 31821\}$ ms and $dp = \{0, 190, 310, 311, 510, 1000\}$ μm respectively. The experimental setup of Section 5.1 was used to acquire 90 samples with 30 frames each with dimensions of 650×480 pixels and the CNR was calculated in the periphery of the blood vessels to measure the impact of the factors to compare the awK, sawK, aawK, aK, sdK and asK and their parameters are those described in previous experiments.

In terms of quantitative results, the proposed awK and asK obtained the highest CNRs with an $F = 1401.12$ and $p = 0.00$ with $\alpha = 0.05$ in the analysis performed, leaving the depth and exposure time as blocks. The multiple comparisons indicate that the awK obtained the highest CNR with a mean of 3.39 ± 1.5798 followed by

the sawK with a mean of 2.64 ± 1.1549 (Fig. 5.11). The analysis performed by depth suggests that the improvement is more significant at low depths than at the deeper, but the improvement is still substantial according to the multiple comparisons with two factors with $\alpha = 0.05$. The improvement in the CNR at shallow depths is because the pixel selection is better when no combined pixels are in the periphery of the blood vessels. This complies with the decrease in CNR when the depth increases as the combined pixels in images with higher depths.

Contrary the aawK, the proposed methods sawK and sawK obtained a higher CNR. The effects in the statistical model obtained an F-score of 31976.20, 15908.62, and 375.77 for the method, depth, and exposure time, being the method the principal factor that influences the CNR with a p-value of 0.00. On the other hand, the pairwise comparison of the method and the exposure time indicates that the results are statistically significant among methods and exposure time. The means and deviation for all the factors are shown in Fig. 5.12.

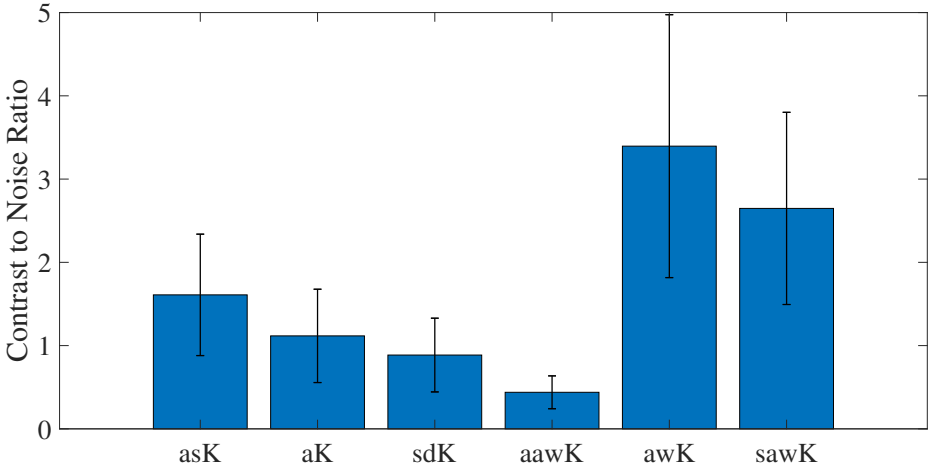
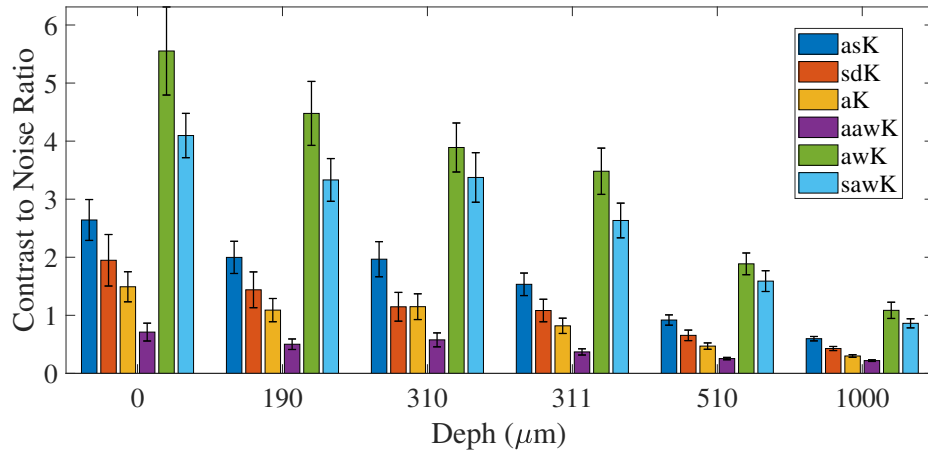
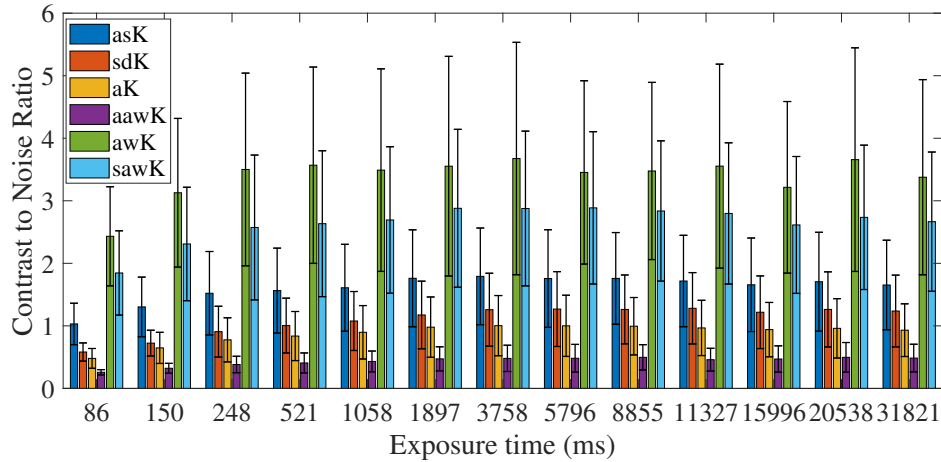


Figure 5.11: Comparison of the contrast to noise ratio grouped by methods.

Last, having established the statistical significance, an analysis of the effect caused by exposure time and depth were performed for the awK and the sawK. The analysis shows that the exposure time does not significantly impact the higher depths for the proposed methods. But in contrast, at superficial depths, the exposure



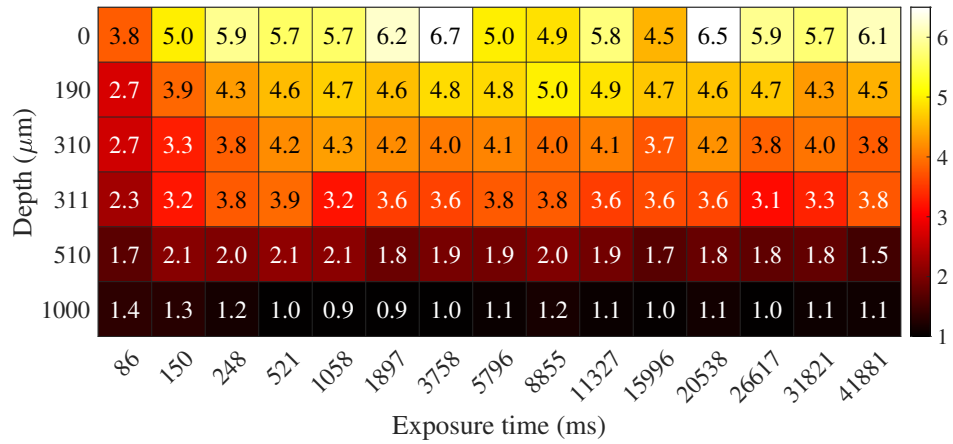
(a) *in-vitro*



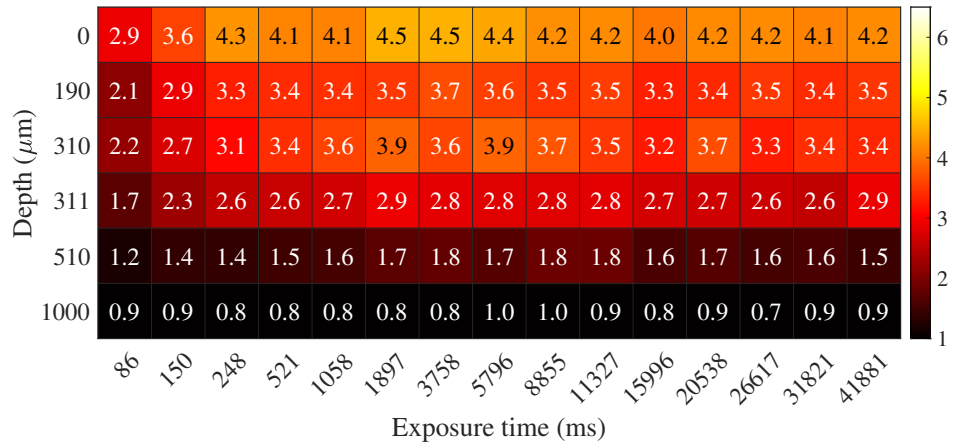
(b) *in-vivo*

Figure 5.12: Comparisons of the CNR grouped by a) method and b) exposure time.

time can play an essential role in the quality of the CIs. This behavior means that the adaptive methods can outperform the traditional methods even at low exposure times, but in the case of superficial depths, the quality of the image can be improved using high exposure times (Fig. 5.13).



(a)



(b)

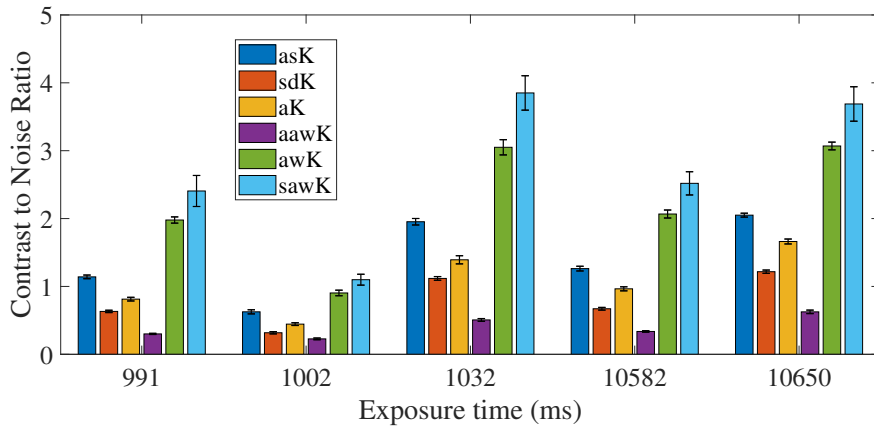
Figure 5.13: Comparison of the contrast to noise ratio varying the exposure time and depth for the a) awK and b) sawK.

5.6 Performance of the approaches varying the blood flow

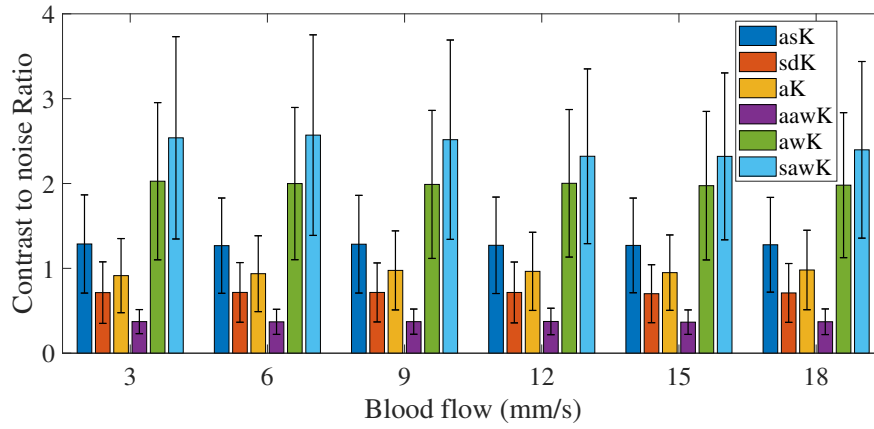
Movement in the capillaries is the main reason because the LSCI technique can be useful to locate blood vessels due to the blurring pattern that is generated by the momentum transfer of particles in motion. For this reason, among others, an experiment was performed to know the effect of the blood flow velocity in the quality of the CIs obtained via adaptive processing. The main factor of study in this experiment is the blood flow velocity which took values $v = \{3, 6, 9, 12, 15, 18\}$ mm/s in the *in-vitro* images. Also, the exposure times of $et = \{991, 1002, 1032, 10582, 10650\}$

ms and $dp = \{0, 310, 1000, 10182\} \mu m$ were studied as factors to analyze the results under different environments.

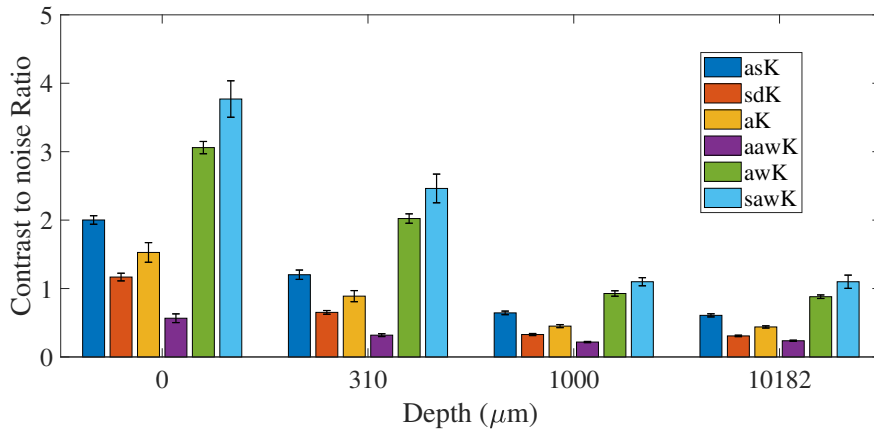
The awK and the sdK obtained the highest CNR for all the factors involved with a F-score = 1981.72 and p-value = 0.00. In contrast, the blood flow does not play an important role in the results, with an F-score = 1.29 and a p-value = 0.26. Thus, the adaptive processing obtained a significant result for all the exposure times, depths, and blood flows. The results are backed by pairwise Tukey comparisons with $\alpha = 0.05$, and the results are depicted in Fig. 5.14.



(a)



(b)



(c)

Figure 5.14: Comparison of the contrast to noise ratio varying the blood flow grouped by a) exposure time, b) blood flow and c) depth.

5.7 Segmentation results

In this section, for the segmentation of blood vessels, the images used for the validation and experimentation consist of simulated straight blood vessels for the *in-vitro* RSI set and a set of *in-vivo* images from the dorsal of a rat as described in the experimental setup section (Sec. 5.1) in previous works of the investigation group. For the *in-vitro* RSIs 7 depths were analyzed 0, 200, 400, 500, 600, 700, 900 μm and different contrast methods to test for invariance to the contrast method. To assess the performance of the method, we used the Jaccard Index (JI) in the periphery of the blood vessels as an evaluation metric because most of the image is tissue, and metrics such as Rand Index (RI) or Accuracy may provide a biased evaluation. The results were separated into two groups for comparison; the first group represents the JI for the segmentation models trained with a traditional feature extraction using a squared analysis window with a $d = 5$. The second group consists of the results obtained with the adaptive feature extraction using adaptive analysis windows to extract the features of each pixel in the RSI. The training set is divided into two slices; the first one consists in 70% of the samples for training and 30% left for validation to train a K-NN classification model for simplicity with eight features, the sum, max, min value, mean, range, standard deviation and entropy. For replication, 10-folds cross-validation was used for the training samples. The statistical factors are described in Table 5.5.

Table 5.5: Factors of the experiments.

Factor	Levels	Value
Depth	8	0, 200, 400, 500, 600, 700, 900
Contrast method	4	asK,aK,sdK,awK,sawK,
Features	2	traditional, adaptive
Classification model	1	k-NN

The solution demonstrates to be viable at different depths and independently of the contrast method employed (Fig. 5.15a). Therefore, the adaptive feature extraction method may be invariable to the reference image used. The results measured as JI showed that the adaptive feature extraction method could improve the segmentation rates by dismissing small blood outside of the blood vessels and improving the classification of pixels in the periphery, which means that the method can obtain an improved spatial resolution.

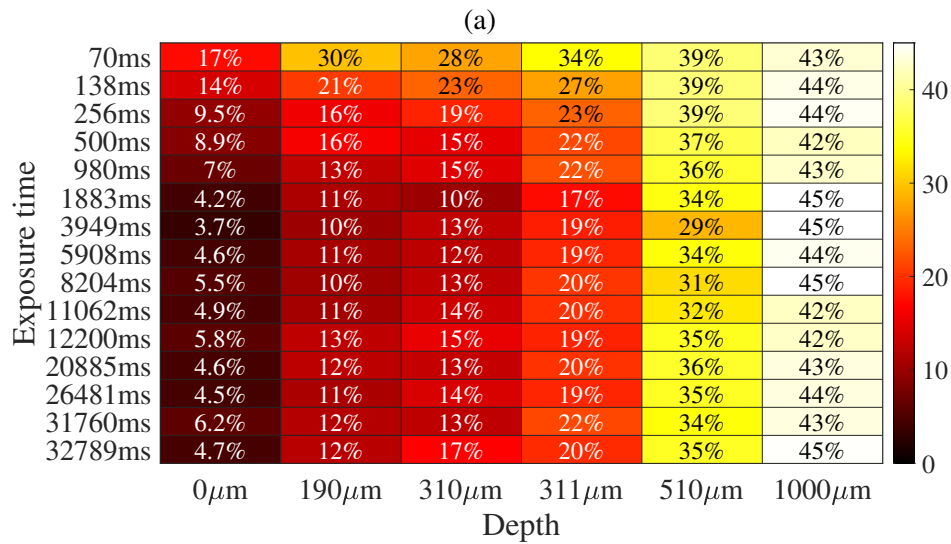
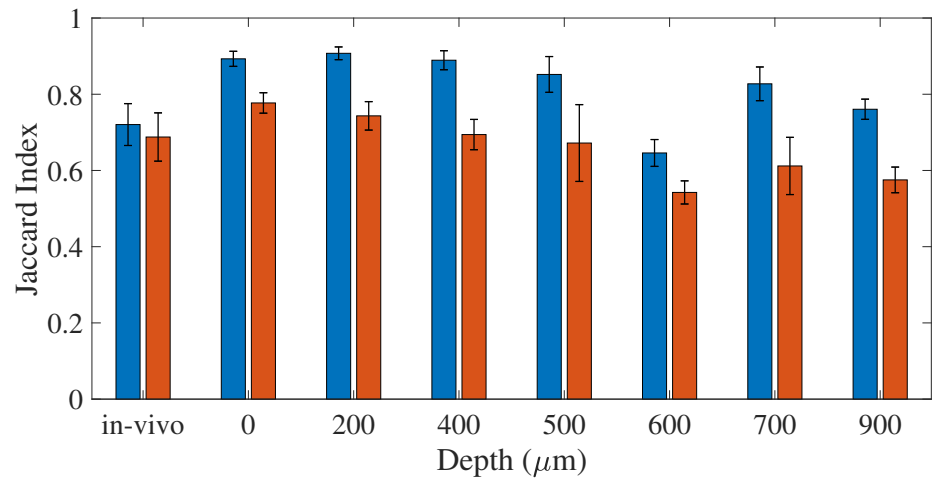


Figure 5.15: Comparison of traditional (red) and adaptive feature extraction(blue) at different depths, a) results grouped by depths and b) improvement heatmap of adaptive methods compared with the traditional methods.

Fig. 5.16 shows some segmentation results, Figs. 5.16a and 5.16c represent the results of the adaptive method and 5.16b and 5.16f show the results of the traditional method. The images show a cropped region of an *in-vivo* sample. Overall, the segmentation results show good performance for both approaches. On the other hand, the adaptive method shows that the segmentation has two interesting properties that could explain the improvement in the JI of the adaptive feature extraction. The Observations show that the periphery of the blood vessels is well defined in the adaptive processing because the true positive pixels are closer to the boundaries. Also, small blobs are dismissed in the segmentation results because the images are less noisy.

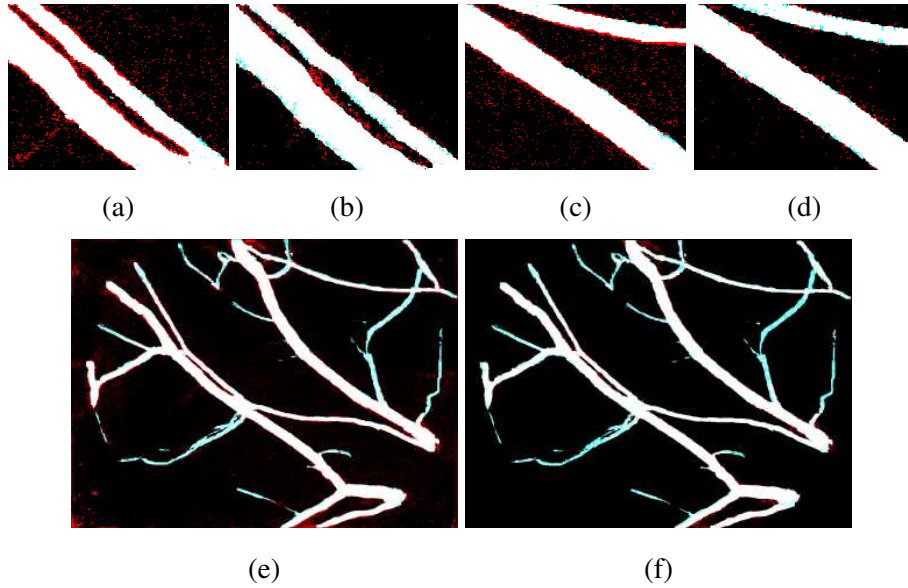


Figure 5.16: Segmentation comparison between the awK method for feature extraction (b) and (d) and the traditional method using squared analysis windows (a) and (c). The black pixels are the true negatives, white are the true positives, red the false negatives and blue the false positives.

Chapter 6

Conclusions and future work

The proposed methods awK and sawK aim to select the pixels involved in the contrast calculation, which means that the size and shape of the pixel selection may vary according to the analyzed region. Thus, it is possible to improve the CIs quality without losing the definition of the relevant structures in the image because more pixels are involved in the contrast calculation. Several experiments were carried out to know the behavior of the proposed methods in various cases.

Adaptive processing in LSCI shows that it is possible to improve the quality of the images under different conditions of depths. It would be logical to think that it is possible to increase the CNR only by using larger analysis windows in the classical approaches, but this introduces a bias in the measurements. Although the CNR may increase if it is measured in the periphery of the blood vessel, in reality, it decreases.

But, the methods show that it is possible to increase the contrast between the static and dynamic regions by measuring the CNR in the periphery of the blood vessels to avoid a bias. In addition, the proposed method improves the quality of the images under different conditions of depth, exposure time, and blood flow. Also, the temporal resolution was improved, obtaining higher CNR values even using one

frame.

Therefore, when a CI is obtained from one frame in terms of visualization, it has the same quality as an image processed with a higher quantity of frames but with improved spatial and temporal resolution. In terms of qualitative evaluation, the CIs not only has reduced noise and improved resolution between regions to differentiate the periphery of the blood vessels from the static region but also, these methods do not introduce artifacts in the image. On the other hand, the segmentation results show that it is possible to extend the method not only to calculate a contrast representation from the RSIs but also to calculate features in an adaptive way for discrimination purposes. A classification model trained with adaptively extracted features can improve the classification rates by avoiding a posterizing effect. How methods like classification with superpixels or using the duality of the structural element do [18].

The proposed methods use the advantages of unsupervised learning to select with anticipation the limits between regions in noisy images, which is the limitation of current adaptive processing methods. These methods have problems with images with noise and outlier values or use thresholds that are difficult to determine in this domain. Although the proposed methods work well in CIs, further analysis may be required to use the methods in images with several objects in the image.

Bibliography

- [1] A. Humeau-Heurtier, P. Abraham, and G. Mahé, “Analysis of laser speckle contrast images variability using a novel empirical mode decomposition: Comparison of results with laser doppler flowmetry signals variability,” *IEEE Transactions on Medical Imaging*, vol. 34, no. 2, 2015.
- [2] I. Fredriksson, M. Larsson, and T. Strömberg, “Measurement depth and volume in laser Doppler flowmetry,” *Microvascular Research*, vol. 78, pp. 4–13, 6 2009.
- [3] A. M. Siegel, D. A. Boas, J. J. Stott, and J. P. Culver, “Volumetric diffuse optical tomography of brain activity,” *Optics Letters*, Vol. 28, Issue 21, pp. 2061-2063, vol. 28, pp. 2061–2063, 11 2003.
- [4] M. S. D. Smith, E. F. Packulak, and M. G. Sowa, “Development of a laser speckle imaging system for measuring relative blood flow velocity,” in *Proceedings of SPIE - The International Society for Optical Engineering*, vol. 6343 I, pp. TeraXion, Canada; Developpement economique Canada,, 2006.
- [5] S. Ogawa, T. M. Lee, A. R. Kay, and D. W. Tank, “Brain magnetic resonance imaging with contrast dependent on blood oxygenation,” *Proceedings of the National Academy of Sciences of the United States of America*, vol. 87, no. 24, pp. 9868–9872, 1990.
- [6] J. S. Paul, A. R. Luft, E. Yew, and F.-S. Sheu, “Imaging the development of an ischemic core following photochemically induced cortical infarction in rats using

- Laser Speckle Contrast Analysis (LASCA),” *NeuroImage*, vol. 29, pp. 38–45, 1 2006.
- [7] W. J. Moy, S. J. Patel, B. S. Lertsakdadet, R. P. Arora, K. M. Nielsen, K. M. Kelly, and B. Choi, “Preclinical in vivo evaluation of Npe6-mediated photodynamic therapy on normal vasculature,” *Lasers in Surgery and Medicine*, vol. 44, no. 2, pp. 158–162, 2012.
- [8] M. Draijer, E. Hondebrink, T. Van Leeuwen, W. Steenbergen, T. v. Leeuwen, W. Steenbergen, T. Van Leeuwen, and W. Steenbergen, “Review of laser speckle contrast techniques for visualizing tissue perfusion.,” *Lasers in medical science*, vol. 24, pp. 639–51, 7 2009.
- [9] M. Nagahara, Y. Tamaki, M. Araie, and T. Umeyama, “The acute effects of stellate ganglion block on circulation in human ocular fundus,” *Acta Ophthalmologica Scandinavica*, vol. 79, no. 1, pp. 45–48, 2001.
- [10] J. Flammer, S. Orgül, V. P. Costa, N. Orzalesi, G. K. Krieglstein, L. M. Serra, J.-P. Renard, and E. Stefánsson, “The impact of ocular blood flow in glaucoma,” *Progress in retinal and eye research*, vol. 21, no. 4, pp. 359–393, 2002.
- [11] D. D. Postnov, V. V. Tuchin, and O. Sosnovtseva, “Estimation of vessel diameter and blood flow dynamics from laser speckle images,” *Biomedical Optics Express*, vol. 7, no. 7, p. 2759, 2016.
- [12] C. Regan, J. C. Ramirez-San-Juan, and B. Choi, “Photothermal laser speckle imaging,” *Optics Letters*, vol. 39, p. 5006, 9 2014.
- [13] C. Regan, C. Hayakawa, and B. Choi, “Momentum transfer Monte Carlo for the simulation of laser speckle imaging and its application in the skin,” *Biomedical Optics Express*, vol. 8, no. 12, p. 5708, 2017.

- [14] K. Basak, G. Dey, M. Mahadevappa, M. Mandal, and P. K. Dutta, “in vivo laser speckle imaging by adaptive contrast computation for microvasculature assessment,” *Optics and Lasers in Engineering*, vol. 62, pp. 87–94, 11 2014.
- [15] J. D. Briers and S. Webster, “Laser speckle contrast analysis (LASCA): a non-scanning, full-field technique for monitoring capillary blood flow,” *Journal of Biomedical Optics*, vol. 1, p. 174, 4 1996.
- [16] P. G. Vaz, A. Humeau-Heurtier, E. Figueiras, C. Correia, and J. Cardoso, “Laser Speckle Imaging to Monitor Microvascular Blood Flow: A Review,” *IEEE Reviews in Biomedical Engineering*, vol. 9, pp. 106–120, 2016.
- [17] L. Winchester and N. Chou, “Blood velocity measurements using laser speckle imaging,” in *The 26th Annual International Conference of the IEEE Engineering in Medicine and Biology Society*, vol. 3, pp. 1252–1255, IEEE, 2004.
- [18] A. Landström and M. J. Thurley, “Adaptive morphology using tensor-based elliptical structuring elements,” *Pattern Recognition Letters*, vol. 34, no. 12, pp. 1416–1422, 2013.
- [19] W. Verkruysse, B. Choi, J. R. Zhang, J. Kim, and J. S. Nelson, “Thermal depth profiling of vascular lesions: Automated regularization of reconstruction algorithms,” *Physics in Medicine and Biology*, vol. 53, pp. 1463–1474, 3 2008.
- [20] J. Kim, J. Oh, and B. Choi, “Magnetomotive laser speckle imaging.,” *Journal of biomedical optics*, vol. 15, no. 1, p. 011110, 2010.
- [21] T. Son, J. Yoon, C.-Y. Ko, Y.-H. Lee, K. Kwon, H. S. Kim, K. J. Lee, and B. Jung, “Contrast enhancement of laser speckle skin image: use of optical clearing agent in conjunction with micro-needling,” in *Journal of the Optical Society of Korea, Vol. 17, Issue 1, pp. 86-90*, vol. 17, p. 68420E, Optical Society of Korea, 2 2008.

- [22] Y. Wang, D. Wen, X. Chen, Q. Huang, M. Chen, J. Lu, and P. Li, “Improving the estimation of flow speed for laser speckle imaging with single exposure time,” *Optics Letters*, vol. 42, no. 1, pp. 57–60, 2017.
- [23] C. Perez-Corona, “Space-directional Laser Speckle Contrast Imaging to Improve Blood Vessels Visualization,” 2018.
- [24] H. Peregrina-Barreto, E. Perez-Corona, J. Rangel-Magdaleno, R. Ramos-Garcia, R. Chiu, and J. C. Ramirez-San-Juan, “Use of kurtosis for locating deep blood vessels in raw speckle imaging using a homogeneity representation,” <https://doi.org/10.1117/1.JBO.22.6.066004>, vol. 22, p. 066004, 6 2017.
- [25] S. A. Rosales-Nunez, H. Peregrina-Barreto, J. Rangel-Magdaleno, J. C. Ramirez-San-Juan, and I. Terol-Villalobos, “Automatic scale determination for adaptive windowing in Laser Speckle Imaging,” 2018.
- [26] J. Serra, “INTRODUCTION TO MATHEMATICAL MORPHOLOGY.,” *Computer vision, graphics, and image processing*, vol. 35, pp. 283–305, 9 1986.
- [27] R. M. Haralick, S. R. Sternberg, and X. Zhuang, “Image Analysis Using Mathematical Morphology,” *IEEE Transactions on Pattern Analysis and Machine Intelligence*, vol. PAMI-9, no. 4, pp. 532–550, 1987.
- [28] V. Ćurić, A. Landström, M. J. Thurley, and C. L. Luengo Hendriks, “Adaptive mathematical morphology - A survey of the field,” *Pattern Recognition Letters*, vol. 47, pp. 18–28, 2014.
- [29] A. Landström, M. J. Thurley, and H. Jonsson, “Adaptive morphological filtering of incomplete data,” in *2013 International Conference on Digital Image Computing: Techniques and Applications, DICTA 2013*, 2013.
- [30] R. Lerallut, [U+FFFD] Decencière, and F. Meyer, “Image filtering using morphological amoebas,” *Image and Vision Computing*, vol. 25, no. 4 SPEC. ISS., pp. 395–404, 2007.

- [31] V. Morard, E. Decencière, P. Dokládál, and E. ere, “Region Growing Structuring Elements and New Operators based on their Shape,” *Signal and Image Processing*, no. Sip, pp. 78–85, 2011.
- [32] J. Debayle and J.-C. Pinoliécole, “SPATIALLY ADAPTIVE MORPHOLOGICAL IMAGE FILTERING USING INTRINSIC STRUCTURING ELEMENTS,” Tech. Rep. 3, 2005.
- [33] H. Wang, L. Dai, Y. Cai, X. Sun, and L. Chen, “Salient object detection based on multi-scale contrast,” *Neural Networks*, vol. 101, pp. 47–56, 5 2018.
- [34] B. Fulkerson, D. Michie, D. J. Spiegelhalter, and C. C. Taylor, “Machine Learning, Neural and Statistical Classification,” *Technometrics*, vol. 37, p. 459, 11 1995.
- [35] S. P. Lloyd, “Least Squares Quantization in PCM,” *IEEE Transactions on Information Theory*, vol. 28, no. 2, pp. 129–137, 1982.
- [36] M. S. Nixon and A. S. Aguado, “Feature Extraction and Image Processing,” *Academic Press*, p. 88, 2008.
- [37] A. Rege, J. Senarathna, N. Li, and N. V. Thakor, “Anisotropic processing of laser speckle images improves spatiotemporal resolution,” *IEEE transactions on bio-medical engineering*, vol. 59, pp. 1272–1280, 5 2012.
- [38] P. G. Vaz, A. Humeau-Heurtier, E. Figueiras, C. Correia, and J. Cardoso, “Performance analysis of spatial laser speckle contrast implementations,” in *BIOINFORMATICS 2017 - 8th International Conference on Bioinformatics Models, Methods and Algorithms, Proceedings; Part of 10th International Joint Conference on Biomedical Engineering Systems and Technologies, BIOSTEC 2017*, vol. 3, pp. 148–153, SciTePress, 2017.

- [39] K. Basak, M. Manjunatha, and P. K. Dutta, “Review of laser speckle-based analysis in medical imaging,” *Medical & Biological Engineering & Computing*, vol. 50, pp. 547–558, 6 2012.
- [40] A. Humeau-Heurtier, G. Mahé, and P. Abraham, “Microvascular blood flow monitoring with laser speckle contrast imaging using the generalized differences algorithm,” *Microvascular Research*, vol. 98, 2015.
- [41] E. Werkmeister, H. Kerdjoudj, L. Marchal, J. F. Stoltz, and D. Dumas, “Multi-photon microscopy for blood vessel imaging: New non-invasive tools (Spectral, SHG, FLIM),” in *Clinical Hemorheology and Microcirculation*, vol. 37, pp. 77–88, IOS Press, 1 2007.
- [42] G. Xi, N. Cao, W. Guo, D. Kang, Z. Chen, J. He, W. Ren, T. Shen, C. Wang, and J. Chen, “Label-free imaging of blood vessels in human normal breast and breast tumor tissue using multiphoton microscopy,” *Scanning*, vol. 2019, 2019.
- [43] F. Lopez-Tiro, H. Peregrina-Barreto, J. Rangel-Magdaleno, and J. C. Ramirez-San-Juan, “Visualization of in-vitro blood vessels in contrast images based on discrete wavelet transform decomposition,” vol. 2019-May, Institute of Electrical and Electronics Engineers Inc., 5 2019.
- [44] D. D. Postnov, X. Cheng, S. E. Erdener, and D. A. Boas, “Choosing a laser for laser speckle contrast imaging,” *Scientific Reports*, vol. 9, no. 1, 2019.
- [45] V. Dremin, E. Zherebtsov, A. Bykov, A. Popov, A. Doronin, and I. Meglinski, “Influence of blood pulsation on diagnostic volume in pulse oximetry and photoplethysmography measurements,” *Applied Optics*, vol. 58, p. 9398, 12 2019.
- [46] A. F. Fercher and J. D. Briers, “Flow visualization by means of single-exposure speckle photography,” *Optics Communications*, vol. 37, pp. 326–330, 6 1981.

- [47] S. M. S. Kazmi, S. Baliai, and A. K. Dunn, "Optimization of camera exposure durations for multi-exposure speckle imaging of the microcirculation," *Biomedical Optics Express*, vol. 5, p. 2157, 7 2014.
- [48] F. Lopez-Tiro, H. Peregrina-Barreto, J. Rangel-Magdaleno, J. C. Ramirez-San-Juan, and J. M. Ramirez-Cortes, "Effect of the exposure time in laser speckle imaging for improving blood vessels localization: A wavelet approach," in *I2MTC 2020 - International Instrumentation and Measurement Technology Conference, Proceedings*, Institute of Electrical and Electronics Engineers Inc., 5 2020.
- [49] B. Choi, C. Regan, and J. C. Ramirez-San-Juan, "Photothermal laser speckle imaging," *Optics Letters*, Vol. 39, Issue 17, pp. 5006-5009, vol. 39, pp. 5006–5009, 9 2014.
- [50] C. Bernard, T. Wenbin, and J. Wangcun, "The Role of Laser Speckle Imaging in Port-Wine Stain Research: Recent Advances and Opportunities," vol. 4, no. 11, pp. 1–32, 2017.
- [51] B. Jung, J. Lee, and T. Son, "Contrast Enhancement of Laser Speckle Contrast Image in Deep Vasculature by Reduction of Tissue Scattering," *Journal of the Optical Society of Korea*, Vol. 17, Issue 1, pp. 86-90, vol. 17, pp. 86–90, 2 2013.
- [52] R. Godinho, M. Silva, J. Nozela, and R. Braga, "Online biospeckle assessment without loss of definition and resolution by motion history image," *Optics and Lasers in Engineering*, vol. 50, pp. 366–372, 3 2012.
- [53] M. A. Davis, S. M. S. Kazmi, and A. K. Dunn, "Imaging depth and multiple scattering in laser speckle contrast imaging," *Journal of Biomedical Optics*, vol. 19, no. 8, 2014.
- [54] M. Z. Ansari, A. Humeau-Heurtier, N. Offenhauser, J. P. Dreier, and A. K. Nirala, "Visualization of perfusion changes with laser speckle contrast imaging

- using the method of motion history image,” *Microvascular Research*, vol. 107, pp. 106–109, 9 2016.
- [55] R. Arizaga, N. L. Cap, H. J. Rabal, and M. Trivi, “Display of local activity using dynamical speckle patterns,” *Optical Engineering*, vol. 41, p. 287, 2 2002.
- [56] H. Fujii, K. Nohira, Y. Shintomi, T. Asakura, and T. Ohura, “Blood flow observed by time-varying laser speckle,” *Optics Letters*, vol. 10, p. 104, 3 1985.
- [57] H. Peregrina-Barreto, J. A. Arias-Cruz, J. C. Ramirez-San-Juan, R. Chiu, R. Ramos-Garcia, and T. Spezzia-Mazzocco, “Visualization of in vitro deep blood vessels using principal component analysis based laser speckle imaging,” *Biomedical Optics Express*, Vol. 10, Issue 4, pp. 2020-2031, vol. 10, pp. 2020–2031, 4 2019.
- [58] J. D. Briers and S. Webster, “Laser speckle contrast analysis (LASCA): a non-scanning, full-field technique for monitoring capillary blood flow,” <https://doi.org/10.1117/12.231359>, vol. 1, pp. 174–179, 4 1996.
- [59] J. Qiu, “Spatiotemporal laser speckle contrast analysis for blood flow imaging with maximized speckle contrast,” *Journal of Biomedical Optics*, vol. 15, p. 016003, 1 2010.
- [60] D. D. Duncan and S. J. Kirkpatrick, “Spatio-temporal algorithms for processing laser speckle imaging data,” in *Optics in Tissue Engineering and Regenerative Medicine II* (S. J. Kirkpatrick and R. K. Wang, eds.), vol. 6858, p. 685802, SPIE, 2 2008.
- [61] D. Briers, D. D. Duncan, E. Hirst, S. J. Kirkpatrick, M. Larsson, W. Steenbergen, T. Stromberg, and O. B. Thompson, “Laser speckle contrast imaging: theoretical and practical limitations,” *Journal of Biomedical Optics*, vol. 18, p. 066018, 6 2013.

- [62] D. A. Boas, S. Sakadžić, J. Selb, P. Farzam, M. A. Franceschini, and S. A. Carp, “Establishing the diffuse correlation spectroscopy signal relationship with blood flow.,” *Neurophotonics*, vol. 3, p. 031412, 7 2016.
- [63] H. Cheng and T. Q. Duong, “Simplified laser-speckle-imaging analysis method and its application to retinal blood flow imaging,” *Optics Letters*, vol. 32, p. 2188, 8 2007.
- [64] H. Cheng, Q. Luo, S. Zeng, S. Chen, J. Cen, and H. Gong, “Modified laser speckle imaging method with improved spatial resolution,” *Journal of Biomedical Optics*, vol. 8, no. 3, p. 559, 2003.
- [65] C. S. Chen, J. L. Wu, and Y. P. Hung, “Theoretical aspects of vertically invariant gray-level morphological operators and their application on adaptive signal and image filtering,” *IEEE Transactions on Signal Processing*, vol. 47, pp. 1049–1060, 4 1999.
- [66] J. C. Ramirez-San-Juan, C. Regan, B. Coyotl-Ocelotl, and B. Choi, “Spatial versus temporal laser speckle contrast analyses in the presence of static optical scatterers,” *Journal of Biomedical Optics*, vol. 19, p. 106009, 10 2014.
- [67] K. Basak, G. Dey, M. Mahadevappa, M. Mandal, and P. K. Dutta, “in vivo laser speckle imaging by adaptive contrast computation for microvasculature assessment,” *Optics and Lasers in Engineering*, vol. 62, pp. 87–94, 11 2014.
- [68] R. Lerallut, [U+FFFD] Decencière, and F. Meyer, “Image Filtering Using Morphological Amoebas,” in *Mathematical Morphology: 40 Years On*, pp. 13–22, Springer Science & Business Medi, 7 2005.
- [69] R. Verdú-Monedero, J. Angulo, and J. Serra, “Anisotropic morphological filters with spatially-variant structuring elements based on image-dependent gradient fields,” *IEEE Transactions on Image Processing*, vol. 20, no. 1, pp. 200–212, 2011.

- [70] V. Curic, C. L. Hendriks, and G. Borgefors, “Saliency adaptive structuring elements,” *IEEE Journal on Selected Topics in Signal Processing*, vol. 6, no. 7, pp. 809–819, 2012.
- [71] J. Renan Velazquez-Gonzalez, H. Peregrina-Barreto, J. Rangel-Magdaleno, and J. C. Ramirez-San-Juan, “Robust laser speckle contrast images suitable for blood vessel visualization,” *2017 IEEE International Autumn Meeting on Power, Electronics and Computing, ROPEC 2017*, vol. 2018-Janua, no. Ropec, pp. 1–6, 2017.
- [72] E. Postnikov, M. Tsoy, and D. Postnov, “MATLAB for laser speckle contrast analysis (LASCA): A practice-based approach,” *Progress in Biomedical Optics and Imaging - Proceedings of SPIE*, vol. 10717, no. April, 2018.
- [73] J. R. Velazquez-Gonzalez, H. Peregrina-Barreto, J. Rangel-Magdaleno, and J. C. Ramirez-San-Juan, “Robust laser speckle contrast images suitable for blood vessel visualization,” in *2017 IEEE International Autumn Meeting on Power, Electronics and Computing (ROPEC)*, no. Ropec, pp. 1–6, IEEE, 11 2017.
- [74] H.-Y. Jin, N. V. Thakor, and H.-C. Shin, “Laser Speckle Contrast Analysis Using Adaptive Window,” in *13th International Conference on Biomedical Engineering*, pp. 444–447, Berlin, Heidelberg: Springer Berlin Heidelberg, 2009.
- [75] J. A. Arias-Cruz, C. E. Perez-Corona, H. Peregrina-Barreto, R. Ramos-Garcia, and J. C. Ramirez-San-Juan, “Visualization of deep blood vessels in speckle imaging using homogeneity measurement of the co-occurrence matrix,” vol. 9660, no. August 2015, p. 96601O, 2015.
- [76] L. Song, Z. Zhou, X. Wang, X. Zhao, and D. S. Elson, “Simulation of speckle patterns with pre-defined correlation distributions,” *Biomedical Optics Express*, vol. 7, no. 3, p. 798, 2016.

- [77] B. Jung, J. Lee, and T. Son, “Contrast Enhancement of Laser Speckle Contrast Image in Deep Vasculature by Reduction of Tissue Scattering,” *Journal of the Optical Society of Korea*, Vol. 17, Issue 1, pp. 86-90, vol. 17, pp. 86–90, 2 2013.
- [78] V. Kalchenko, A. Sdobnov, I. Meglinski, Y. Kuznetsov, G. Molodij, and A. Harmelin, “A robust method for adjustment of laser speckle contrast imaging during transcranial mouse brain visualization,” 7 2019.
- [79] H. Peregrina-Barreto, E. Perez-Corona, J. Rangel-Magdaleno, R. Ramos-Garcia, R. Chiu, and J. C. Ramirez-San-Juan, “Use of kurtosis for locating deep blood vessels in raw speckle imaging using a homogeneity representation,” *Journal of Biomedical Optics*, vol. 22, p. 066004, 6 2017.
- [80] A. Aminfar, N. Davoodzadeh, G. Aguilar, and M. Princevac, “Application of optical flow algorithms to laser speckle imaging,” *Microvascular Research*, vol. 122, pp. 52–59.
- [81] D. D. Postnov, J. Tang, S. E. Erdener, K. Kılıç, and D. A. Boas, “Dynamic light scattering imaging,” *Science Advances*, vol. 6, p. eabc4628, 11 2020.
- [82] B. Choi, N. M. Kang, and J. S. Nelson, “Laser speckle imaging for monitoring blood flow dynamics in the in vivo rodent dorsal skin fold model,” *Microvascular Research*, vol. 68, pp. 143–146, 9 2004.
- [83] R. B. Saager, C. Kondru, K. Au, K. Sry, F. Ayers, and A. J. Durkin, “Multilayer silicone phantoms for the evaluation of quantitative optical techniques in skin imaging,” <https://doi.org/10.1117/12.842249>, vol. 7567, pp. 40–47, 2 2010.